

# Formulating and Deploying Strength Amplification Controllers for Lower-Body Walking Exoskeletons

Gray C. Thomas<sup>1,\*</sup>, Orion Campbell<sup>2</sup>, Nick Nichols<sup>2</sup>, Nicolas Brissonneau<sup>3</sup>,  
Bingham He<sup>3</sup>, Joshua James<sup>2</sup>, Nicholas A. Paine<sup>2</sup> and Luis Sentis<sup>3,\*</sup>

<sup>1</sup> The University of Michigan, USA

<sup>2</sup> Apptronik Inc., USA

<sup>3</sup> The Human Centered Robotics Lab, The University of Texas at Austin, Austin, USA

Correspondence\*:

Gray Thomas / Luis Sentis

gcthomas@umich.edu / lsentis@austin.utexas.edu

## 2 ABSTRACT

3 Augmenting the physical strength of a human operator during unpredictable human-directed  
4 (volitional) movements is a relevant capability for several proposed exoskeleton applications,  
5 including mobility augmentation, manual material handling, and tool operation. Unlike controllers  
6 and augmentation systems designed for repetitive tasks (e.g. walking), we approach physical  
7 strength augmentation by a task-agnostic method of force amplification—using force/torque  
8 sensors at the human–machine interface to estimate the human task force, and then amplifying  
9 it with the exoskeleton. We deploy an amplification controller that is integrated into a complete  
10 whole-body control framework for controlling exoskeletons that includes human-led foot transitions,  
11 inequality constraints, and a computationally efficient prioritization. A powered lower-body  
12 exoskeleton is used to demonstrate behavior of the control framework in a lab environment.  
13 This exoskeleton can assist the operator in lifting an unknown backpack payload while remaining  
14 fully backdrivable.

## 1 INTRODUCTION

15 Exoskeletons offer the potential to greatly augment the physical load carrying ability by placing the strength  
16 of machines under the dexterous control of people. But the amplification of strength through force sensor  
17 feedback remains a challenging problem in practice. This problem is unique to this application area and  
18 is rarely discussed with regard to the various other types of exoskeletons—*e.g.* those that aim to recover  
19 locomotion capability lost to disease (Kwa et al., 2009; Agrawal et al., 2017), offload the strenuous work  
20 of rehabilitation therapy from therapists (Sugar et al., 2007; Kim and Deshpande, 2017), or aid healthy  
21 locomotion with timed power boosts (Mooney et al., 2014; Zhang et al., 2017; Sawicki et al., 2020).  
22 Amplification control systems are designed to magnify the physical strength of the operator as he or she  
23 interacts with a load *through the exoskeleton*, while also reducing the weight and inertia the operator feels  
24 from the exoskeleton itself. This kind of control allows non-repetitive, unpredictable tasks with unknown  
25 payloads.

26 Lifting *known* payloads is a simpler problem. These loads can be lifted by directly compensating  
27 their nominal weight with actuator torque commands (*i.e.* the “gravity compensation” strategy). This  
28 compensation could be lifting mostly the exoskeleton itself (Kazerooni et al., 2005), or even offloading  
29 the operator’s own bodyweight (Kong et al., 2010; Lv et al., 2018; Lin et al., 2019). In an exoskeleton  
30 system that can be easily backdriven by the operator, gravity compensation alone is a practical approach  
31 for lifting well-modeled payloads (Campbell, 2018). However, the operator must still accelerate the full  
32 inertia, compensate for any model error, and lift any extra payloads. The inertia burden can be lessened by  
33 adding positive acceleration feedback (Kazerooni, 2005; Kong and Tomizuka, 2009), but all three issues  
34 can be addressed by adding force-feedback-based amplification.

35 Admittance control for exoskeletons (Yu and Rosen, 2013; Fontana et al., 2014; Jacobsen and Olivier,  
36 2014; Lecours et al., 2012) uses force sensor feedback at the human interface<sup>1</sup> in order to increase the  
37 human-side closed-loop admittance, reduce sensitivity to the mass model, and lift unknown loads. But the  
38 admittance ‘increase’ is relative to the admittance controller’s plant: a position-controlled robot. Since  
39 position-controlled robots have an artificially low admittance to begin with (Yu and Rosen, 2013; Gonzalez  
40 and Asada, 2019), the closed-loop human-side admittance is typically not an improvement over the torque-  
41 controlled gravity compensation strategy. Additionally, the position-controlled plant of the admittance  
42 controller will attenuate all external forces acting on the robot. This has the disadvantage of depriving the  
43 operator of the force feedback they would normally perceive when they interact with the load.

44 In order to allow bidirectional transmission of forces to coexist with amplification of human strength,  
45 the exoskeleton must transmit both amplified forces from the user to the load and attenuated forces from  
46 the load to the user. And this requires a force sensor configuration that can distinguish between load-  
47 and human-originated forces. Directly measuring a robot–load interface and robot–human interface with  
48 force sensors allowed (Kazerooni and Guo, 1993; Kazerooni and Mahoney, 1991a,b) to control *disparate*  
49 admittance behaviors for each interface.<sup>2</sup> But the controller from (Kazerooni and Guo, 1993) was still not  
50 designed to improve the human-side admittance relative to the torque-controlled gravity compensation  
51 strategy. It still used admittance control and a position-controlled robot. In this paper, we use force sensing  
52 at the human–exoskeleton and actuator–exoskeleton interfaces (*i.e.* series elastic actuators), and this  
53 serves the dual purposes of distinguishing the human from the load and allowing torque control at the  
54 joints. The two interface admittances are then shaped with a cascade of amplification feedback on top of  
55 torque-controlled actuators.<sup>3</sup>

56 Unfortunately, the problem of non-passivity is inherent to feedback control that conceals inertia. This is  
57 an issue regardless of how the inertia was concealed—through positive acceleration feedback (Kazerooni,  
58 2005) or force feedback (Buerger and Hogan, 2007). Without passivity, we must fall back to robust  
59 control in order to certify such behaviors. Most importantly, the exoskeleton’s human-facing port—its  
60 force–position relationship at the human–exoskeleton interface—will be in a feedback interconnection with  
61 the human’s exoskeleton-facing port. Studies of this feedback interconnection (Kazerooni, 1990; Buerger  
62 and Hogan, 2007, 2006; He et al., 2019) and the human in particular (He et al., 2019; He et al., 2020) have  
63 modeled the human as a mass-spring-damper system with a range of parameter values. The most variable  
64 parameter is stiffness, as this depends on muscle contraction (Hogan, 1984). We must demonstrate that no  
65 possible human behavior leads to instability—a robust control problem. Designing a machine to be passive

<sup>1</sup> Measuring human muscular effort, as can also be accomplished via electromyography (muscle measurement) (Kawamoto and Sankai, 2005; Young and Ferris, 2016).

<sup>2</sup> The HARDIMAN I exoskeleton (Makinson et al., 1969) attempted to do this as well, but with a flawed approach that neglected multi-joint coordination.

<sup>3</sup> Our reaction-force sensing series elastic actuators are torque controlled based on disturbance observers (Paine et al., 2014; Paine, 2014).

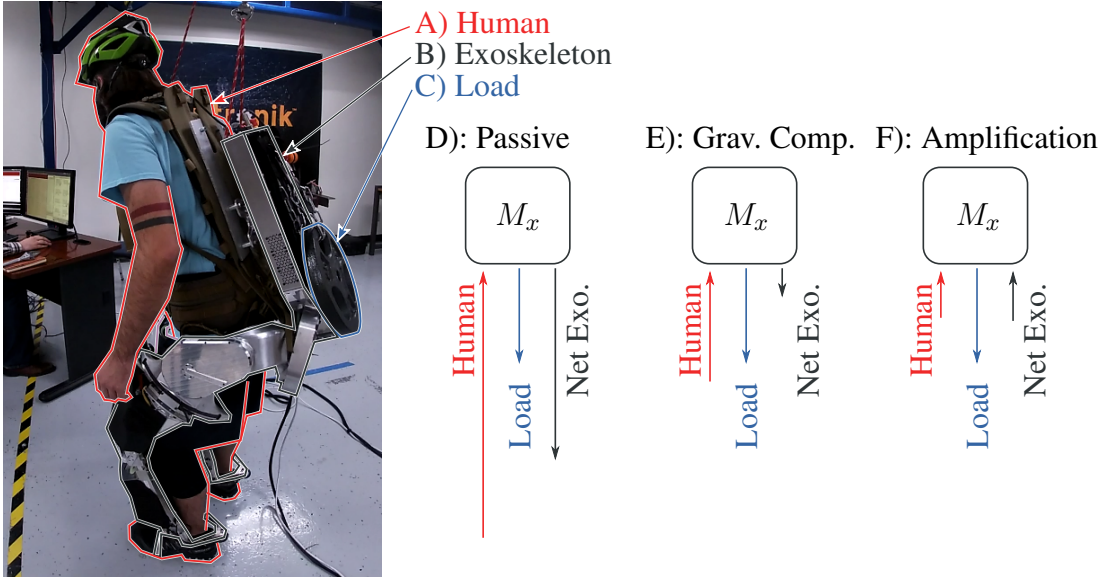


**Figure 1.** Human–exoskeleton–load interaction illustrating the concept of amplification. Marker A, the Human (inc. part of the backpack), connects to B, the Apptronik Sagittarius Exoskeleton, which connects to C, the unknown Load. The Human–Exoskeleton connection is force/torque sensitive to allow human force feedback. Three diagrams represent forces acting on the inertia matrix of the exoskeleton  $M_x$  in static equilibrium. When the exoskeleton is in zero-torque mode, the human supports both the load and the gravitational weight of the exoskeletons (D). When the exoskeleton compensates gravity, the human needs only compensate the load and the gravity compensation error (E). Amplification improves on this by making the exoskeleton augment the human input, in addition to compensating gravity (F).

66 (Colgate and Hogan, 1988; Hogan, 1989; Colgate and Brown, 1994; Adams and Hannaford, 1999) can also  
 67 be seen as a robust control problem: such designs guarantee stability against a very wide range of ‘human’  
 68 behaviors—the set of all passive transfer functions. Our prior work (Thomas et al., 2019; He et al., 2019;  
 69 He et al., 2019; He et al., 2020) has studied this stability problem for a table-mounted elbow exoskeleton.

70 In this paper, we deploy an amplification controller on a 12 degree of freedom (12-DOF) lower-body  
 71 exoskeleton with 8 torque-controlled active joints and 4 passive (but sensorized) joints (Fig. 1). The  
 72 core framework of this controller is a multi-joint coordination approach modeled after humanoid robot  
 73 controllers for torque-controlled joints (Sentis et al., 2010; Kim et al., 2016) (e.g. the Valkyrie robot at  
 74 NASA JSC (Radford et al., 2015; Paine et al., 2015)) in which a list of ‘tasks’ (e.g. the position of the end  
 75 effector, or the force between the feet) is accomplished by the robot. The full controller comprises (a) an  
 76 optimization that determines robot joint torques using a *prioritized* list of tasks and a set of constraints that  
 77 act on the sum of human and robot torques—the ‘Shared-Body Controller’ (Sec. 5); (b) a six degree of  
 78 freedom (6-DOF) task that constrains the robot to follow human-led footstep transitions—the *inter-foot*  
 79 force task (Sec. 4); (c) an amplification task that accomplishes strength amplification in Cartesian space  
 80 (Sec. 2); and (d) a heuristic tuning strategy for the amplification filter, which is based on (He et al., 2019)  
 81 and (Thomas et al., 2019) (Sec. 3). We demonstrate the deployed controller’s ability to reduce the human  
 82 effort necessary to lift the robot itself and an unknown payload, as well as the operator’s ability to easily  
 83 back-drive the system to walk around and climb some stairs (Sec. 6).

Symbol	Meaning
$M_x, B_x, g_x$	exoskeleton mass matrix, Coriolis vector, and gravity vector
$\ddot{q}, \dot{q}, q$	exoskeleton joint acceleration, velocity, and position vectors
$\tau$	exoskeleton joint torque vector
$J_h, f_h$	human interaction cuff Jacobian, forces
$J_l, f_l$	load interaction Jacobian, forces
$J_t, x_t$	task Jacobian, position
$\bar{J}_t$	dynamically <b>consistent</b> pseudo-inverse of $J_t$
$\Lambda_t$	Task-space inertia matrix
$\hat{f}_t$	desired task force
$\alpha$	human strength amplification rate
$\hat{f}_a$	Ideal (infinite bandwidth) desired amplification force
$\hat{f}_a(t), \hat{F}_a(s)$	desired amplification task force vector (time domain, frequency domain)
$f'_h(t), F'_h(s)$	transformed human force (time domain, frequency domain)
$K(s)$	Force feedback filter

**Table 1.** Nomenclature for Sec. 2

## 2 STRENGTH AMPLIFICATION TASK

84 Strength amplification can be illustrated using the example of an ideal fixed-base (arm-like) “exoskeleton”  
 85 performing a force-feedback behavior with an end effector in contact with both the human and some load.

86 Consider a fully actuated, grounded base exoskeleton acted on by both a human operator (Jacobian  $J_h$ ,  
 87 and force  $f_h$ ) and an unknown load (Jacobian  $J_l$ , and force  $f_l$ ) (list of symbols in Tab. 1),

$$M_x(q)\ddot{q} + B_x(q, \dot{q}) + g_x(q) = \tau + J_h^T f_h + J_l^T f_l. \quad (1)$$

88 The exoskeleton measures the human forces,  $f_h$ , and can use this measurement to specify  $\tau$ . As we will  
 89 see, by implementing an amplifying control law, the exoskeleton can reduce the human’s perception of the  
 90 load. However to define this amplification law, we will need to first introduce the concept of a whole-body  
 91 control task (Sentis et al., 2010).

92 Whole body control tasks describe behaviors we want a robot to achieve, for example moving an end  
 93 effector to a desired 6-DOF pose in Cartesian space. While this task constrains 6-DOF, it could equivalently  
 94 be divided into sub-components, e.g. a 3-DOF position task and a 3-DOF orientation task. **Singularity-prone**  
**kinematics are not necessarily reflected in the tasks. Rather, the tasks are goals that may not always be**  
 95 **possible to satisfy given the constraints of the robot.** Tasks can also specify the desired internal forces of  
 96 multi-contact (Kim et al., 2016). More generally, tasks define both an effort-flow port of the robot and a  
 97 target behavior for the robot to imitate at that port—a spring-damper behavior for position control and a  
 98 force behavior for force control. This port is known as the task-space. By using the mapping between the  
 99 joint-space of the robot and the task-space (and the mapping’s Jacobian,  $J_t$ ), a whole-body controller can  
 100 implement the task behaviors even while floating in zero gravity or maintaining contact with arbitrarily  
 101 shaped ground (Sentis et al., 2010).

103 We define the amplification task to reduce human perception of load and exoskeleton dynamics  
 104 disturbances in the task space. These task-space dynamics are originally (*i.e.* in open-loop) found by

105 premultiplying (1) by  $(J_t M_x^{-1} J_t^T)^{-1} J_t M_x^{-1}$ , yielding

$$\Lambda_t(\ddot{x}_t - \dot{J}_t \dot{q}) + \bar{J}_t^T(B_x + g_x) = \bar{J}_t^T(\tau + J_h^T f_h + J_l^T f_l), \quad (2)$$

106 where  $\Lambda_t = (J_t M_x^{-1} J_t^T)^{-1}$  is the task-space mass matrix and  $\bar{J}_t = M_x^{-1} J_t^T \Lambda_t$  is the dynamically  
107 consistent pseudo-inverse of the task Jacobian (Kim et al., 2016). The amplification task specifies only a  
108 linear subspace of the torque vector,  $\bar{J}_t^T \tau$ , as

$$\bar{J}_t^T \tau = \hat{f}_a + \bar{J}_t^T(g_x), \text{ where } \hat{f}_a = (\alpha - 1) \bar{J}_t^T J_h^T f_h. \quad (3)$$

109 Here, the first term  $\hat{f}_a$  represents a desired force amplifying the human operator's strength, and the second  
110 term compensates gravity. Reduced human perception of load and exoskeleton dynamic disturbances can  
111 be seen in the closed-loop task-space,

$$\frac{1}{\alpha} \Lambda_t(\ddot{x}_t - \dot{J}_t \dot{q}) + \frac{1}{\alpha} \bar{J}_t^T(B_x) = \bar{J}_t^T J_h^T f_h + \frac{1}{\alpha} \bar{J}_t^T J_l^T f_l. \quad (4)$$

112 While the human term stays the same, every other term is reduced. Equivalently, we could say these  
113 closed-loop dynamics amplify the influence of the human force by a factor of  $\alpha$ . But this behavior is  
114 complicated by the matrices  $\bar{J}_t^T J_h^T$  and  $\bar{J}_t^T J_l^T$ , which represent projection onto the space of the task as  
115 well as the potential for mismatch between the reference frames of the task, the human-measuring cuff  
116 interface, and the load.

117 In the special case where the human and load forces act *only* in the task-space and the human and load  
118 forces are expressed in the units and reference frame of the task-space (*i.e.*  $J_t = J_h = J_l$ ), this simplifies  
119 to

$$\Lambda_t(\ddot{x}_t - \dot{J}_t \dot{q}) + \bar{J}_t^T(B_x) = \alpha f_h + f_l, \quad (5)$$

120 which clearly shows the human advantage with respect to the load, inertia, and Coriolis forces. For example,  
121 this case occurs if (1) both forces are applied to one sensorized, 6-DOF end effector; (2) the sensor  
122 measurements of the spatial force vectors of the human and the load are all converted to the same reference  
123 frame (Featherstone, 2014); and (3) this frame is also the frame in which the task is expressed.

124 This law is unfortunately an unobtainable ideal, because it changes the apparent inertia the human feels  
125 instantaneously. In other words, the law requires that the actuation bandwidth is infinite. Beyond the  
126 actuation bandwidth, all feedback systems asymptotically revert to their natural dynamics. Thus, in the  
127 limit as frequency approaches infinity, the frequency-domain representation of exoskeleton torque should  
128 be zero.

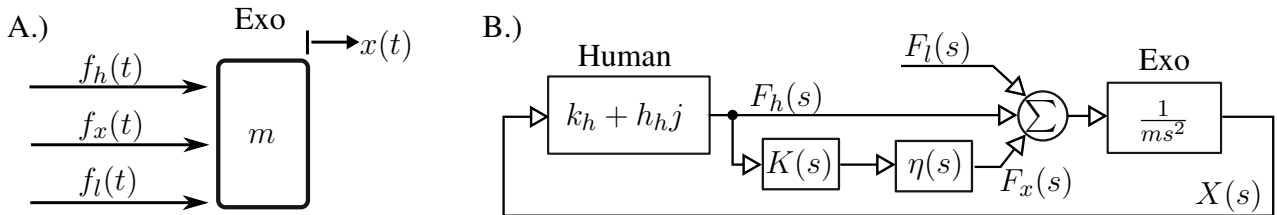
## 129 2.1 Filtered Amplification Task

130 To allow for bandwidth limited amplification tasks, we introduce the notion of filtered force feedback  
131 amplification. Instead of an amplification task following Eq. (3), we define a desired filtered amplification  
132 force as the result of a frequency domain filter as

$$\hat{f}_a(s) = K(s) F'_h(s), \quad \text{where} \quad f'_h(t) = \bar{J}_t^T J_h^T f_h, \quad (6)$$

133  $f'_h$  is the human force vector represented in the task space,  $F'_h(s)$  is its Laplace transform, and  $K(s)$  is  
134 some matrix of linear filters analogous to  $(\alpha - 1)$  in the ideal case. We design this matrix of filters to be  
135 diagonal, and consider a strategy for tuning the diagonal filter elements in Sec. 3.

Symbol	Meaning
$m$	one-DOF exoskeleton mass
$k_h + h_{hj}$	human complex stiffness (see (He et al., 2020))
$x(t), X(s)$	one-DOF position (time-domain, frequency-domain)
$f_l(t), F_l(s)$	load force
$f_x(t), F_x(s)$	exoskeleton actuator force
$f_h(t), F_h(s)$	human force
$\hat{\alpha}(s)$	desired amplification transfer function
$\alpha(s)$	realized amplification transfer function
$K(s)$	feedback controller transfer function
$\eta(s)$	actuation imperfections (time-delay, low-pass filtering)
$\omega_a$	amplification bandwidth (tuning parameter)
$\alpha_0$	steady-state amplification rate
$\zeta$	amplification damping ratio

**Table 2.** Nomenclature for Sec. 3**Figure 2.** Amplification filter tuning model, a one-DOF mass ( $m$ ) acted upon by human ( $f_h$ ), exoskeleton actuator ( $f_x$ ), and load ( $f_l$ ) forces (A). Closed loop system resulting from complex stiffness human mechanical impedance and exoskeleton amplification with bandwidth-limiting time-delay and low pass filter effects in  $\eta(s)$  (B).

136 In our exoskeleton, the *amplification task* is a 6-DOF task concerning the exoskeleton's hip/backpack  
 137 frame and the 6-axis force/torque sensor that connects the hip/backpack link to the operator. The vector  
 138  $F'_h(s)$  is the 6-axis force/torque sensor measurement's expression in the task frame (the exoskeleton's hip  
 139 frame). And  $\hat{F}_a(s)$  is the desired *amplification task* spatial force vector (expressed in hip frame), which  
 140 will be treated as a time-domain vector signal  $\hat{f}_a(t)$  in Sec. 5.

### 3 TUNING THE AMPLIFICATION FILTERS

141 Since ideal amplification cannot be attained, we must consider a design space of more realistic amplification  
 142 behaviors. And the essence of this design space is a bandwidth limitation on the control. This bandwidth  
 143 limit, and its impact on coupled human-exoskeleton stability, has been studied in the context of single  
 144 degree of freedom exoskeleton systems (He et al., 2019; Thomas et al., 2019; Huang et al., 2020; He et al.,  
 145 2020), and we will use the single degree of freedom case as a heuristic for understanding the tuning of  
 146 the amplification task's  $K(s)$  filter elements in our multi-DOF exoskeleton. While this heuristic omits  
 147 several obvious nonlinear effects and inter-task couplings in the full system, it captures the basic problem  
 148 of human-exoskeleton instability that can occur when bandwidth limits are ignored.

#### 149 3.1 Human-Exoskeleton Stability Model

150 Consider a 1-DOF linear human and exoskeleton system (Fig. 2.A, Tab. 2) where the exoskeleton acts  
 151 like an inertia  $M$  and is being acted upon by three forces: the human  $f_h(t)$ , the actuator  $f_x(t)$ , and the load

152  $f_l(t)$  as

$$m\ddot{x}(t) = f_l(t) + f_h(t) + f_x(t), \quad (7)$$

153 where  $x(t)$  the shared position of the human and the exoskeleton. We write this model in the frequency  
154 domain as

$$ms^2X(s) = F_l(s) + F_h(s) + F_x(s), \quad (8)$$

155 using capitalization to distinguish Laplace transforms from time-domain versions of the same signal.

156 The force-feedback filter  $K(s)$  is based on a nominal amplification behavior  $\hat{\alpha}(s) = 1 + K(s)$ .<sup>4</sup> We  
157 parameterize the desired amplification transfer function as

$$\hat{\alpha}(s) = \frac{s^2 + 2\zeta\omega_z s + \omega_z^2}{s^2 + 2\zeta\omega_p s + \omega_p^2}, \quad (9)$$

158 i.e. a second order lag with two conjugate poles at lower frequency than the two conjugate zeros, using the  
159 same  $\zeta$  twice for convenience, though this could potentially be optimized. While this  $\hat{\alpha}(s)$  is not strictly  
160 causal, it produces a  $K(s)$  which is:

$$K(s) = \hat{\alpha}(s) - 1 = \frac{2\zeta(\omega_z - \omega_p)s + \omega_z^2 - \omega_p^2}{s^2 + 2\zeta\omega_p s + \omega_p^2}. \quad (10)$$

161 Actuation imperfections ultimately limit the bandwidth, and we model these as the transfer function  $\eta(s)$ .  
162 They include a time delay  $T$  and low pass filter effect (i.e. the closed loop bandwidth of the actuator's  
163 torque controller) at frequency  $\omega$  with damping ratio  $\zeta$ ,

$$\eta(s) = e^{-Ts} \frac{\omega^2}{s^2 + 2\zeta\omega + \omega^2}. \quad (11)$$

164 The mechanical impedance of the human is also modeled as a complex stiffness—a spring with a  
165 dissipation term that does not change with frequency. (This model can be interpreted as similar to a spring  
166 with a coulomb friction term that scales with the magnitude of deflection, such that the energy lost in  
167 flexing the spring does not depend on the speed of the flexing (Brissonneau et al., 2021).) This complex  
168 stiffness model is more accurate than the viscous damping model in predicting human energy dissipation in  
169 the elbow, especially at low frequencies (He et al., 2020).

170 To facilitate easy tuning of our controller we **reparameterize** in terms of an amplification bandwidth  
171 parameter  $\omega_a$  (equal to  $\omega_p$ ) and a low frequency amplification gain  $\alpha_0 \geq 1$  (equal to  $\omega_z^2/\omega_p^2$ ) so that

$$K(s) = \frac{2\zeta(\sqrt{\alpha_0} - 1)\omega_a s + (\alpha_0 - 1)\omega_a^2}{s^2 + 2\zeta\omega_a s + \omega_a^2}. \quad (12)$$

172 We then tune only the amplification bandwidth  $\omega_a$ .

### 173 3.2 Tuning $\omega_a$

174 The tuning process we propose is simple. Sufficiently low values of  $\omega_a$  are always stable, so we can  
175 increase  $\omega_a$  until instability to tune the system without explicit system identification.

---

<sup>4</sup> We reserve the symbol  $\alpha(s)$  for the realized amplification behavior, which includes the effect of actuator imperfections  $\eta(s)$ .

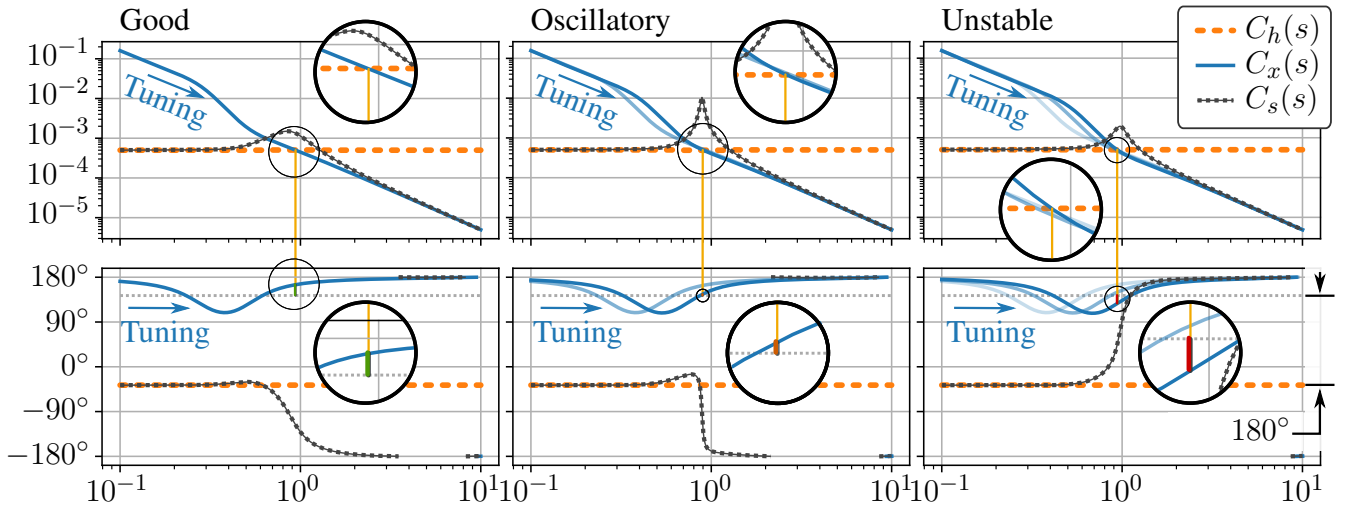


**Figure 3.** One parameter tuning of the amplification filter. Three bode plots show three different tuning configurations as the single tuning parameter (the amplification bandwidth  $\omega_a$ ) is increased to failure in our frequency domain model. Tuning arrows indicate increasing  $\omega_a$ . Plotted are the (integral) admittance of the human,  $C_h(s) = 1/(K_h + C_h j)$ , the human-side admittance of the exoskeleton,  $C_x(s) = 1/(\alpha(s)Ms^2)$ , and the admittance of the closed loop system obtained when the two are interconnected in parallel,  $C_s(s) = X(s)/F_l(s)$ . Note that in the third plot, the phase of the closed loop system rises instead of falling, indicating an unstable pole in the right half of the complex plane. In all three bode plots, magnification is used to highlight the calculation of a “Human Phase Margin” which predicts this instability. This calculation uses the phase of  $C_x(s)$  at the frequency where the magnitude of  $C_x(s)$  is equal to the magnitude of  $C_h(s)$ —the crossover frequency. At this frequency, stability of the resulting human–exoskeleton interconnection is determined by comparing the phase of  $C_x(s)$  to a reference phase  $180^\circ$  offset from the phase of  $C_h(s)$ . The difference between the phase of  $C_x(s)$  and this reference is the “Human Phase Margin.”

176 The bode plot of  $X(s)/F_l(s)$  (‘System’ in Fig. 3) transitions from a stable low-pass filter behavior to an  
 177 unstable system as  $\omega_a$  is increased. We note that the critical frequency satisfies a relationship akin to zero  
 178 phase margin, where both the magnitude of the human (integral) admittance,  $1/(K_h + C_h j)$  (‘Human’ in  
 179 Fig. 3), is equal to that of the amplified exoskeleton admittance,  $1/(\alpha(s)Ms^2)$  (‘Robot’ in Fig. 3), and the  
 180 phases of the two are offset by  $180^\circ$ . We call the phase angle difference  $\angle C_x(j\omega) - \angle C_h(j\omega) - 180^\circ$  at  
 181 crossover frequency  $\omega$  where  $|C_x(j\omega)| = |C_h(j\omega)|$  the ‘Human Phase Margin’. Since the human phase  
 182 margin is also the phase margin for the open loop transfer function  $C_x(s)C_h^{-1}(s)$  (in the unit negative  
 183 feedback case), the human phase margin predicts the stability of the closed loop system resulting from the  
 184 human–exoskeleton interconnection.

185 A single tuning experiment can determine the limiting bandwidth for any particular amplification shape.  
 186 Starting with  $\omega_a$  very low, we slowly scale it up until the system appears to vibrate. Once the threshold of  
 187 oscillation is found, the oscillation frequency is roughly the crossover frequency, and we could obtain an  
 188 estimate of the human phase if we had a good model of the torque tracking performance and time delay.  
 189 The problem is practically solved, however, by the formulation of the controller in a one-parameter tunable  
 190 way. With one knob, it is easy to increase the performance up to the limit, back off for robustness, and get a  
 191 good result in the end.

### 192 3.3 Practical Considerations

193 Ultimately this model is introduced as a heuristic for the tuning behavior occurring in the more complex  
 194 exoskeleton system, so we now revisit its assumptions with an eye to the realistic case.

195 If a small value for  $\alpha_0$  is selected such that the minimum phase of  $1/(\hat{\alpha}(s)Ms^2)$  stays above the gray  
 196 line in Fig. 3, the system will be stable even for very high  $\omega_a$ . However, this will not hold true forever,  
 197 and the bandwidth limiting factors in  $\eta(s)$  will cause the realized behavior  $1/(\alpha(s)Ms^2)$  itself to become  
 198 unstable for high values of  $\omega_a$ .

199 The human model considered here neglected human inertia. If this term were added, the human inertia  
 200 would be roughly comparable to the inertia of the exoskeleton. The model would not be changed at low  
 201 frequencies, so the base case (stability of low  $\omega_a$ ) of our tuning process would stay the same. The lower  
 202 phase of the human due to the inertia would improve the maximum allowable  $\omega_a$ , but a limit would still  
 203 exist due to the bandwidth limiting factors in  $\eta(s)$ .

204 The inertia of the exoskeleton changes as the person moves it, and this means that the stability of the  
 205 amplification behavior can change depending on the configuration. Practically, this means that when tuning  
 206 for maximum performance, care will need to be taken to test each iteration of the  $\omega_a$  parameter over a wide  
 207 range of poses, to ensure a robust stability.

208 It is well known that humans have the ability to co-contract their antagonistic muscles and artificially raise  
 209 their mechanical impedance, and this represents another changing aspect of this problem. If we assume  
 210 that this scales both  $k_h$  and  $h_h$  together, as supported in (He et al., 2020), then co-contraction will lower  
 211 the human admittance and improve the human phase margin. In fact, this effect has even been exploited to  
 212 improve controller performance online, provided a co-contraction predictor can be learned from wearable  
 213 sensors (e.g. EMG and bicep circumference sensors) (Huang et al., 2020). To ensure robust stability while  
 214 tuning for performance, the operator will need to avoid co-contraction so as to explore the gain-limiting  
 215 case.

## 4 INTER-FOOT FORCE TASK

216 Human-led foot contact transitions, such as walking or shifting balance, are an important part of any scheme  
 217 for controlling lower-body exoskeletons. To allow this critical feature we introduce a second task, the  
 218 *inter-foot force task*, that is achieved simultaneously and causes the exoskeleton to follow human-initiated  
 219 foot lifting.

220 With one foot on the ground, this foot acts as a virtual base for the exoskeleton—a contact constraint on  
 221 its otherwise free-fall dynamics. Since the exoskeleton is not designed to jump, we can assume that some  
 222 sort of virtual base always exists. When two feet are on the ground at the same time, we can imagine a  
 223 virtual single foot between them that acts like a base and moves between the feet according to the operator’s  
 224 own weight distribution.

225 Two feet together have 12-DOF worth of reaction forces, and the virtual single foot contact only allows  
 226 6-DOF to be used as a virtual base. The remaining 6-DOF can be thought of as an error, representing the  
 227 mismatch between the exoskeleton’s reaction force distribution and the operator’s. This error should be  
 228 zero, and eliminating it is the purpose of the *inter-foot force task*.

229 To define this error, we first consider how correct reaction force distribution looks, and then consider  
 230 the linear space of reaction forces perpendicular to this. For this purpose, we introduce an optimization  
 231 problem that optimally distributes a net reaction wrench  $f_s$  into two components, one for each foot,

Symbol	Meaning
$f_i$	foot $i$ 's spatial force vector in frame $i \in \{1, 2\}$
$f$	stacking of $f_1$ and $f_2$
$f_s$	sum of foot spatial force vectors in frame $s$
$Q_1, Q_2, Q$	reaction force cost definition matrices
${}^bX_a^*$	spatial force vector transform, frame $a \rightarrow$ frame $b$
$\lambda$	Lagrange multiplier vector in optimization
$X$	equality constraint matrix in optimization
$\Gamma$	$= [XQ^{-1}X^T]^{-1}$
$\bar{X}$	$= Q^{-1}X^T\Gamma$ , a pseudo-inverse of $X$
$f_d$	<i>inter-foot force task</i> error in frame $d$
$\tilde{X}$	weighted inter-foot difference matrix
$G$	virtual base definition matrix

**Table 3.** Nomenclature for Sec. 4

$$\underset{f_1, f_2}{\text{minimize}} \quad \frac{f_1^T Q_1 f_1}{2} + \frac{f_2^T Q_2 f_2}{2} \quad (13)$$

$$\text{subject to} \quad {}^sX_1^* f_1 + {}^sX_2^* f_2 = f_s, \quad (14)$$

232 where  $Q_1$  and  $Q_2$  are positive definite and typically diagonal. We introduce two new reference frames:  
 233 frame  $s$  (for “sum”), and frame  $d$  (for “difference”). Both frames are weighted averages of the two foot  
 234 frames. Frame  $s$  is approximately matched with the human center of pressure. Frame  $d$  is the mirror image  
 235 of frame  $s$ , and both frames overlap at the mid-foot point when the human puts equal weight on each foot.  
 236 Transformation  ${}^sX_1^*$  converts spatial force vectors from the 1<sup>st</sup> foot's frame to frame  $s$ , and  ${}^sX_2^*$  is the  
 237 same for the other foot. The force  $f_s$  represents the sum of the two foot spatial force vectors expressed in  
 238 frame  $s$  (Tab. 3).

239 The equality constrained quadratic programming problem can be solved analytically. Starting from the  
 240 equilibrium conditions,

$$Qf + X^T\lambda = 0, \quad \text{where,} \quad (15)$$

$$Q = \begin{pmatrix} Q_1 & \\ & Q_2 \end{pmatrix}, \quad (16)$$

$$f = \begin{pmatrix} f_1 \\ f_2 \end{pmatrix}, \quad (17)$$

$$X = \begin{pmatrix} {}^sX_1^* & {}^sX_2^* \end{pmatrix}, \quad \text{and} \quad (18)$$

$$Xf = f_s. \quad (19)$$

241 In matrix form,

$$\begin{pmatrix} Q & X^T \\ X & 0 \end{pmatrix} \begin{pmatrix} f \\ \lambda \end{pmatrix} = \begin{pmatrix} 0 \\ f_s \end{pmatrix}, \quad (20)$$

$$\begin{pmatrix} f \\ \lambda \end{pmatrix} = \begin{pmatrix} Q^{-1} - \bar{X}XQ^{-1} & \bar{X} \\ \bar{X}^T & -\Gamma \end{pmatrix} \begin{pmatrix} 0 \\ f_s \end{pmatrix}, \quad (21)$$

242 where  $\Gamma = [XQ^{-1}X^T]^{-1}$  and  $\bar{X} = Q^{-1}X^T\Gamma$ . Thus

$$f = (Q^{-1}X^T) \cdot [XQ^{-1}X^T]^{-1}f_s, \quad (22)$$

$$\begin{pmatrix} f_1 \\ f_2 \end{pmatrix} = \begin{pmatrix} Q_1^{-1s}X_1^{*T} \\ Q_2^{-1s}X_2^{*T} \end{pmatrix} \cdot [{}^sX_1^*Q_1^{-1s}X_1^{*T} + {}^sX_2^*Q_2^{-1s}X_2^{*T}]^{-1}f_s. \quad (23)$$

243 This 12-DOF solution  $f$  is the virtual single foot contact's distribution of reaction forces between the  
 244 two feet. The other six degrees of freedom in the foot forces—the degrees of freedom not specified by  
 245 constraint (14)—represent the *inter-foot force task* error. More specifically, we define the *inter-foot force*  
 246 *task* error  $f_d$  in frame  $d$  to complete a parameterization of the foot forces  $f$

$$f = \bar{X}f_s + \left[ I - \bar{X}(\bar{X}^T\bar{X})^{-1}\bar{X}^T \right] \tilde{X}^T f_d, \quad (24)$$

247 where we introduce

$$\tilde{X} = \begin{pmatrix} {}^dX_1^{*-1}w_2 \\ -{}^dX_2^{*-1}w_1 \end{pmatrix}, \quad (25)$$

248 as a rough parameterization of the deviation from the desired force distribution. This gets contorted into  
 249 being perpendicular to  $\bar{X}$  by the premultiplication with an  $\bar{X}$  image space nullifier. Ultimately, the *inter-foot*  
 250 *force task* tries to **avoid choosing an exoskeleton torque that results in a nonzero**  $\|f_d\|$ , and when  $f_d = 0$ ,  
 251 reaction forces minimize the previously defined quadratic cost (since  $f = \bar{X}f_s$ ). This leaves  $f_s$  as the path  
 252 of least resistance the optimization uses to hold up the weight of the exoskeleton.

253 We define  $\mathbf{G}$  to simplify notation:

$$f = \mathbf{G} \cdot \begin{pmatrix} f_s \\ f_d \end{pmatrix}, \quad (26)$$

254

$$\mathbf{G} = \left( \bar{X} \quad \left[ I - \bar{X}(\bar{X}^T\bar{X})^{-1}\bar{X}^T \right] \tilde{X}^T \right). \quad (27)$$

255 As mentioned in Sec. I, our exoskeleton controller is tasked with *simultaneously* accomplishing the  
 256 *amplification task* at the hip/backpack interface (Sec. 3) and the *inter-foot force task*. In terms of reaction  
 257 forces, the *amplification task* serves a similar purpose to the centroidal momentum task introduced in  
 258 (Koolen et al., 2016) or the center of mass task in (Sentis et al., 2010): it determines the required *sum*  
 259 of reaction forces. Meanwhile, the *inter-foot force task* (similar to the internal force tasks from (Kim  
 260 et al., 2016)) determines the part of the reaction force vector that is decoupled from the center of mass  
 261 acceleration. With both tasks active, the reaction forces are all defined and the joint torques can be thought  
 262 of as resulting from an inverse dynamics process—as in the Dynamic Balance Force Control of (Stephens  
 263 and Atkeson, 2010).

Symbol	Meaning
$\tau$	optimization variable: joint torque vector
$M_x, B_x, g_x$	exoskeleton mass, Coriolis, gravity
$\ddot{q}, \dot{q}, q$	joint acceleration, velocity, position
$S$	underactuation matrix for a free floating base
$J_h, f_h$	Jacobian for human contact and forces
$J_r, f_r$	Jacobian for ground contact and reaction forces
$C_r, c_r$	reaction force inequality matrix and bias
$e(\cdot)$	a task error function
$\sigma(\cdot)$	a task scalarization function
$s_+, s_-$	1-norm slack variables
$w$	weight vector
$J_a, f_a, \ddot{x}_a$	Jacobian, force, accel. for the <i>amplification task</i>
$J_f, f_f, \ddot{x}_f$	Jacobian, force, accel. for feet
$\mathbf{J}, \mathbf{f}, \mathbf{\ddot{x}}$	Jacobian, force, accel. for composite task
$\bar{\mathbf{J}}$	Dynamically consistent pseudo-inverse of $\mathbf{J}$
$\Lambda$	inertia matrix in composite task frame
$\mathbf{G}$	virtual base definition matrix
$\bar{\tau}$	maximum torque, human + exoskeleton
$\hat{f}_a$	vector of filtered desired <i>amplification task</i> forces from Sec. 2

**Table 4.** Nomenclature for Sec. 5

## 5 WEIGHTED 1-NORM SHARED-BODY CONTROL

264 To combine the *amplification task* and *inter-foot force task* while also respecting limitations on the  
 265 exoskeleton, we compute the joint torques of the exoskeleton using a linear optimization problem. This  
 266 problem uses concepts of contact constraints, prioritization between task sub-components, a weighted  
 267 1-norm cost, and the actuator-mapped reaction force space in order to be computationally efficient.

### 268 5.1 Contact Constraints

269 There is an important caveat to this concept of a virtual single-foot contact. Unlike actual fixed-base  
 270 robots, exoskeletons with feet can topple over. Since an exoskeleton is essentially a humanoid robot (in  
 271 feedback interconnection with a human), the inequality-constrained floating base models (Koolen et al.,  
 272 2016; Kim et al., 2016, 2018; Mungai and Grizzle, 2020) are still relevant to keeping its feet flat on the  
 273 ground. These constraints act on the base–ground reaction forces,  $f_r$ , which are not part of the standard  
 274 *fixed-base* robot model. They are defined by the combination of a *floating-base* exoskeleton and a contact  
 275 constraint:

$$M_x \ddot{q} + B_x + g_x = S\tau + J_h^T f_h + J_r^T f_r + J_l^T f_l, \quad (28)$$

$$J_r \ddot{q} + \dot{J}_r \dot{q} = 0, \quad (29)$$

276 with notation as in Tab. 4. To avoid tilting the feet, sliding the feet, or pulling on the ground, additional  
 277 inequality constraints must be maintained,

$$C_r f_r + c_r \geq 0. \quad (30)$$

278 The inequalities described by  $C_r$  and  $c_r$  are simple approximations of the friction cone: for example, two  
 279 rows would be used to express  $\mu|f_x| \leq f_z$ , where  $\mu$  is the friction coefficient. But the size of  $C_r$  depends

280 on how many feet are on the ground. In addition to these limits due to contact, there are upper bounds to  
 281 the torque magnitude the exoskeleton can provide. And if some of the joints are not actuated, then they  
 282 have an upper limit of zero.

## 283 5.2 Actuator-Mapped Reaction Force Space

284 In order to speed up the solver and increase its accuracy, we reduce the number of free variables in our  
 285 optimization problem by handling some equality constraints in advance. This is not necessary theoretically,  
 286 as the problem is not actually changed by handling these constraints, however attempts to lean on the  
 287 solver's own ability to perform linear algebra resulted in disappointing precision and speed. Thus, we found  
 288 the need to quickly re-express reaction forces as functions of joint torque.

289 More specifically, we find  $(f_a(\tau)^T, f_f(\tau)^T)^T$ —the mapping from the 12-DOF joint torque vector to  
 290 an 18-DOF vector of forces that concatenates the ground reaction forces with the human–exoskeleton  
 291 interaction forces at the backpack.<sup>5</sup> We define a new composite Jacobian,  $\mathbf{J}$ , force vector,  $\mathbf{f}$ , and task  
 292 acceleration,  $\ddot{\mathbf{x}}$ , as

$$\mathbf{J} = \begin{pmatrix} J_a \\ J_f \end{pmatrix}, \quad \mathbf{f} = \begin{pmatrix} f_a \\ f_f \end{pmatrix}, \quad \ddot{\mathbf{x}} = \begin{pmatrix} \ddot{x}_a \\ \ddot{x}_f \end{pmatrix}. \quad (31)$$

293 Beginning with the physical equations (28) and (29), we can reformat the dynamics of the exoskeleton as  
 294 a matrix equality with an analytic solution,

$$\begin{pmatrix} M_x & \mathbf{J}^T \\ \mathbf{J} & 0 \end{pmatrix} \begin{pmatrix} \ddot{q} \\ -\mathbf{f} \end{pmatrix} = \begin{pmatrix} -B_x - g_x \\ \ddot{\mathbf{x}} - \dot{\mathbf{J}}\dot{q} \end{pmatrix} + \begin{pmatrix} S \\ 0 \end{pmatrix} \tau, \quad (32)$$

295 which can be solved as in (21). The  $S$  matrix represents the under-actuation due to the floating base  
 296 (under-actuation due to non-actuated mechanical joints is handled separately, through joint torque limits).  
 297 We define the dynamically consistent pseudo inverse of  $\mathbf{J}^T$ ,  $\bar{\mathbf{J}}^T$ , satisfying  $\bar{\mathbf{J}}^T \mathbf{J}^T = I$  (a left inverse), but  
 298 likely *not* satisfying  $\mathbf{J}^T \bar{\mathbf{J}}^T = I$ :

$$\bar{\mathbf{J}}^T = (\mathbf{J} M_x^{-1} \mathbf{J}^T)^{-1} \mathbf{J} M_x^{-1}. \quad (33)$$

299 And we define inertia in the composite task frame  $\Lambda = (\mathbf{J} M_x^{-1} \mathbf{J}^T)^{-1}$ . Together, these allow us to state the  
 300 result,

$$\mathbf{f} = \Lambda \ddot{\mathbf{x}} - \Lambda \dot{\mathbf{J}} \dot{q} + \bar{\mathbf{J}}^T (B_x + g_x) - \bar{\mathbf{J}}^T S \tau. \quad (34)$$

301 Some terms in the previous expression are more significant than others, and some of the less significant  
 302 terms are also corrupted by both imperfect knowledge of the exoskeleton's mass matrix and (filtered)  
 303 differentiation noise inherent in using quantized position sensors to estimate velocity and acceleration  
 304 estimates. We did not notice a significant drawback in switching to a simplified version which represents a  
 305 steady state equilibrium:

$$\mathbf{f} = \bar{\mathbf{J}}^T (g_x - S \tau). \quad (35)$$

306 Of course, if we moved fast enough, these omissions would be noticeable. With this simplification, swinging  
 307 the swing foot very fast should require the operator to resist the centrifugal extension of the knee due to the  
 308 inertia of the exoskeleton. Also, squatting very quickly should result in a non-zero backpack sensor force  
 309 due to the neglected acceleration terms. However, at the speeds we tested these effects were dwarfed by

---

<sup>5</sup> Ultimately we only care about the 12-DOF vector of the *inter-foot force task* error and *amplification task* error,  $(f_a(\tau)^T, f_d(\tau)^T)^T$  but the 18-DOF vector representation was more intuitive to debug. We will use the  $\mathbf{G}$  matrix to obtain  $f_d(\tau)$  from  $f_f(\tau)$  later.

310 other control and mechanical imperfections. We hope that future exoskeletons will achieve such mastery  
 311 over the basic terms that these dynamic terms will regain relevancy.

312 **5.3 Prioritized Tasks**

313 With multiple tasks and inequality constraints, the exoskeleton’s behavior is often over-specified. For  
 314 example, the combination of the lateral (y-axis force) component of the *amplification task*, the mediolateral-  
 315 plane rotation (x-axis torque) component of the *amplification task*, and the stance-foot’s lateral center-of-  
 316 pressure limitation may require a non-zero task error. This is easy to visualize if the exoskeleton’s hip is  
 317 far from the stance foot: the ground reaction force can point toward the hip and avoid rotation, or it can  
 318 point straight up and avoid lateral force, but it cannot do both simultaneously. A more general version  
 319 of this problem is well known in the humanoid robotics community (Bretl and Lall, 2008). This happens  
 320 frequently during dynamic walking. And it demands that we specify not only which tasks we want to  
 321 achieve, but in which order the task sub-components should fail to be satisfied if they conflict in this way.<sup>6</sup>

322 When constraints become active, there is neither an obvious choice for what to give up nor an analytical  
 323 method to optimally decide. However, if we provide a *prioritization* of the task sub-components, then an  
 324 optimal answer exists. This prioritization requires additional parameters—a rank order for each task sub-  
 325 component—but these are relatively few, and easy to understand and adjust. This approach has also been  
 326 used to handle redundancy in task definition even without the limitation of constraints (Sentis et al., 2010).  
 327 When constraints become active, the prioritization approach simply abandons the task sub-components  
 328 one at a time, starting with the least important, until the problem is solvable. The lowest priority task  
 329 sub-components are the ones for which we feel the human will have the easiest time comfortably handling  
 330 the task sub-component failure. In the case of our *amplification task*, this could mean a failure to amplify  
 331 the interaction force and/or a failure to achieve gravity compensation. In the case of our *inter-foot force*  
 332 *task*, it could mean applying a force to the user’s swing foot (failure to gravity compensate) or failing to  
 333 match the user’s desired contact force distribution (failure to transition appropriately, most evident if a foot  
 334 is load-bearing when it should not be).

335 Strict prioritization between the tasks is a mathematically well-defined optimization scheme known as  
 336 lexicographic optimization (Bouyarmane and Kheddar, 2017). Lexicographic problems must be solved as a  
 337 series of related optimization sub-problems. First, the most important cost must be optimized within the  
 338 problem constraints—the first optimization sub-problem. Next, the second most important cost must be  
 339 optimized within both the original problem constraints and a new constraint. This new constraint requires  
 340 that the previously minimized cost for the most important objective stays at its previously determined  
 341 optimal value. With a solution to this second optimization sub-problem, a lexicographic optimization  
 342 would proceed forward one cost at a time, solving optimization sub-problems with an ever-increasing list  
 343 of constraints. And this recursive process will continue until each component of the prioritized list of costs  
 344 has been optimized in its own sub-problem.

345 In our hardware, we could only solve three lexicographic optimization sub-problems within our one  
 346 millisecond real-time control window, so with 12 prioritized task sub-components, a proper lexicographic  
 347 solution was outside the realm of plausibility.

---

<sup>6</sup> After trying both prioritizations, we determined that the operator prefers a failure in x-axis torque balance, even if this causes the exoskeleton’s hip to “wobble” relative to the human’s with every step due to the compliance of the backpack attachment in this degree of freedom.

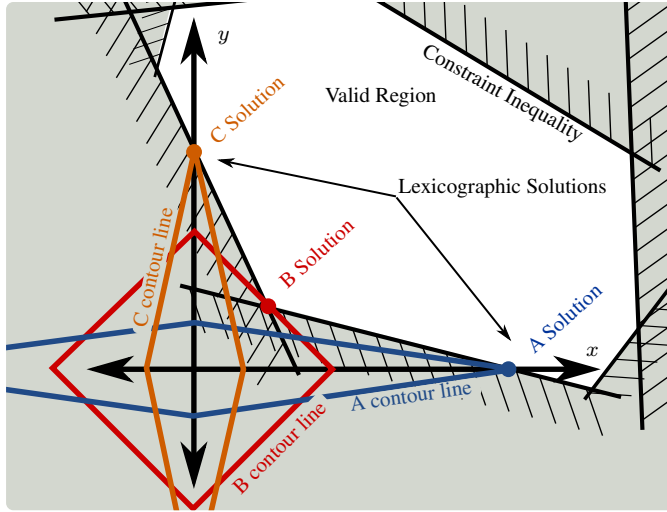


**Figure 4.** Illustration of how weighted 1-norm costs can behave similarly to lexicographic (prioritized) costs. Plot in the space of task error for task- $x$  and task- $y$ . Weighted 1-norm costs A, B, and C are depicted with a single contour line each. Optimal solutions for each task shown as colored circles. The so-called “sparsity promoting” nature of the weighted 1-norm cost can be understood in this context as optimal solutions which sacrifice one task to achieve the other. As exemplified by cost B, however, this is not guaranteed and depends on the inequality constraints and the shape of the valid region they generate.

#### 348 5.4 Weighted 1-Norm Cost

349 Weighted scalarization costs are an established approach to approximating a lexicographic optimization in  
 350 the context of humanoid control (Bouyarmane and Kheddar, 2017). To avoid our computational bottleneck,  
 351 we also used a scalarization that retains the linearity of the cost function. But in doing so we must add  
 352 two positive slack variables and two inequality constraints for each scalarized cost (which were all task  
 353 elements) to remain within a linear programming framework. For our vector of task errors  $e(\tau)$ , we define  
 354 a vector of scalarizations  $\sigma(\tau)$

$$\sigma(\tau) = s_+ + s_- \quad \text{where} \quad s_+ \geq e(\tau), \quad \text{and} \quad s_- \geq -e(\tau), \quad (36)$$

355 where  $s_+$ , and  $s_-$  are the newly introduced vector slack variables, and the new vector inequalities in  
 356 (36) are elementwise inequalities. Under conditions that are almost always met,<sup>7</sup>  $\sigma(\tau) = |e(\tau)|$  (as an  
 357 elementwise absolute value).

358 This approach to modelling an absolute value function within the confines of a linear programming  
 359 problem is the key to our application of a weighted 1-norm cost on the vector of all task errors. Clearly,  
 360 summing the elements of  $\sigma(\tau)$  results in the vector 1-norm of  $e(\tau)$ . Summing the elements of  $\sigma(\tau)$  with  
 361 positive weightings (setting cost equal to  $w^T \sigma(\tau)$  for some vector of positive weights  $w$ ) is a weighted  
 362 scalarization in the sense of (Bouyarmane and Kheddar, 2017), but we can also think of it as a weighted  
 363 1-norm—as the 1-norm for a scaled version of the original space. We prefer this as a name for the way it  
 364 invokes a lozenge-like rhomboid geometry in 2D, and a diagonally-scaled octahedron geometry in 3D.

365 To capitalize on this 2D intuition, Fig. 4 illustrates how the weighted 1-norm cost can be adjusted through  
 366 the weighting to approximate different lexicographic costs (there are only two in 2D space: either  $x$  matters

<sup>7</sup> Specifically that each element of  $\sigma(\tau)$  appears in the cost with a strictly positive weight, and that  $\sigma(\tau)$ ,  $s_-$ , and  $s_+$  are otherwise decoupled from the problem.

more than  $y$  or vice versa). The illustration features a convex 2D set of solutions which satisfy constraints. The two axes represent orthogonal tasks, with the origin representing zero error for both tasks. Cost A uses a weighting that penalizes  $y$  error more than the  $x$ , cost B penalizes them roughly equally, and cost C penalizes  $x$  error more than  $y$ . In both cases A and C, the minimum cost point which satisfies constraints falls on one of the two axes—exactly as a lexicographic solution would. The fact that 1-norm costs tend to produce solution vectors with many zero entries (so-called “sparse” solutions (Candes et al., 2008)) is well known and frequently exploited. To promote *lexicographic solutions* instead of simply solutions with many zeros requires tuning the penalty weights to favor the prioritized tasks. In our illustration, the weightings in A and C are sufficiently extreme, and two lexicographic solutions emerge. Cost B illustrates a non-lexicographic middle-ground: neither cost is penalized enough to completely dominate the other, and the solution vector assigns non-zero error to both tasks.

One disadvantage of weighted 1-norm costs in exoskeleton control is that the constraints are continuously varying due to the changing exoskeleton geometry, and this can cause the optimal behavior to jump discontinuously. This can occur if the 1-norm cost discontinuously switches from being aligned with one lexicographic solution to a different lexicographic solution or even a non-lexicographic solution. We call these abrupt switches “priority inversion events.” To avoid these events entirely, we would need 1-norm weights with near-infinite scale differences between task sub-components. Since this is obviously not possible with floating-point numbers, the weighted 1-norm is an approximation: it sacrifices accuracy for speed. Fortunately, the approximation of the lexicographic problem is asymptotically perfect as the weight discrepancy increases. **We exploited large differences in the weights to avoid priority inversion events during our experiment.** The numerical precision of the linear program solver allowed us sufficient space to set these weights orders of magnitude apart and achieve reliable reproduction of the lexicographic problem in practice. **These numerical limits restrict the total number of priority levels that can be correctly implemented.**

## 5.5 A Linear Program for Shared-Body Control

At this point, we can express the optimization problem that the shared-body controller needs to solve at every controller update. Note that the passive joints<sup>8</sup> are treated as being active joints for the purpose of the optimization. Their non-zero torques represent the expectation of the exoskeleton on the human operator.

We write our optimization problem,

$$\underset{\tau, s_+, s_-}{\text{minimize}} \quad w^T s_+ + w^T s_- \quad (37a)$$

$$\text{subject to} \quad C_r f_r(\tau) \geq 0, \quad (37b)$$

$$\tau \leq \bar{\tau}, \quad -\tau \leq \bar{\tau}, \quad (37c)$$

$$s_+ \geq e(\tau), \quad s_+ \geq 0, \quad (37d)$$

$$s_- \geq -e(\tau), \quad s_- \geq 0, \quad (37e)$$

with some new notation from Tab. 4. Slack variables  $s_+$  and  $s_-$  are introduced to describe absolute value operations. Weightings  $w$  form the weighted 1-norm cost. Limits on absolute torque are expressed with  $\bar{\tau}$ . And the  $\tau$ -dependent vector  $f(\tau)$  from (38) (or from the steady-state approximation (39)) is used to find  $e(\tau)$  and  $f_r(\tau)$ .

<sup>8</sup> The exoskeleton has 2 passive DOFs per leg: ankle inversion/eversion (ankle roll) and internal/external rotation of the hip (hip yaw).

400 The first,  $e(\tau)$ , represents the 12-DOF vector of task errors for the *amplification task* and *inter-foot force task*:

$$e(\tau) = \begin{pmatrix} f_d(\tau) - 0 \\ f_a(\tau) - \hat{f}_a \end{pmatrix}, \quad (38)$$

402 where  $\hat{f}_a$  is the desired amplification task force from (6) in Sec. 2.1;  $f_a(\tau)$  is the force the exoskeleton  
403 applies at the backpack interface, which is a part of  $f(\tau)$  as written in (31); and  $f_d(\tau)$  is also related to  
404  $f(\tau)$  as in (26):

$$\begin{pmatrix} f_s(\tau) \\ f_d(\tau) \end{pmatrix} = \mathbf{G}^{-1} f_f(\tau), \quad (39)$$

405 using the matrix  $\mathbf{G}$  from (27).

406 The second,  $f_r(\tau)$ , represents the subset of the foot forces  $f_f(\tau)$  corresponding to the feet that are actually  
407 on the ground. This vector is used to compute the constraints associated with hard friction cones and  
408 unilateral contacts—i.e. (30), which is directly reproduced in (37b).

409 We call this program “Shared-Body Control” because the human and the exoskeleton’s torque and contact  
410 forces are both relevant. The true conditions for tipping over the foot are a function of both human and  
411 exoskeleton reaction forces. The sum of the human and exoskeleton reaction forces needs to lie within the  
412 friction cone, but sometimes the human works to counterbalance large torques the exoskeleton applies to  
413 the ground. We cannot know the human forces given our sensor configuration, so we are forced to be either  
414 optimistic (risking failure) or very conservative. Taking the conservative route means that our constraint  
415 will occasionally interfere with our tasks unnecessarily.

416 The human is also the only possible source of torques for the passive joints. By relaxing the torque  
417 requirements on the passive joints, the optimization will produce a torque vector representing a sum of  
418 exoskeleton and human originated torques. While we cannot expect the human to implement such torques,  
419 we can use this technique to prevent the exoskeleton from abandoning tasks which it could accomplish  
420 with help from the human (bounded, of course, by  $\bar{\tau}$ ).

## 6 IMPLEMENTATION IN HARDWARE

### 421 6.1 Hardware

422 Our hardware platform is the Sagittarius P5 lower-body exoskeleton from Apptronik Systems, shown in  
423 Fig. 5. This exoskeleton has 12 joints, six per leg. We name the joints in the serial kinematic chain from  
424 the torso to the foot 1) hip abduction/adduction, 2) hip flexion/extension, 3) hip internal/external rotation  
425 (hip yaw), 4) knee flexion/extension, 5) ankle flexion/extension, and 6) ankle pronation/supination (ankle  
426 roll). Of these six, four are powered joints. The two passive joints are hip internal/external rotation (also  
427 referred to as hip yaw for alignment with the local z axis) and ankle pronation/**supination** (which we also  
428 call ankle roll for similar reasons). The powered hip abduction and hip flexion joints are actuated by rotary  
429 series elastic actuators, while the other two feature proprietary linkage designs connecting linear series  
430 elastic actuators with rotary joint motion. Power is provided from off-board the device via a joint power  
431 and communication tether. The actuators communicate with a real-time Linux desktop workstation through  
432 an ethercat bus.

433 The different parts of the exoskeleton are highlighted in Fig. 5, with rigid bodies being bordered by  
434 different color lines on the spectrum from blue to purple, human attachment points in orange, and safety  
435 features in red. To ensure the safety of the operator, the exoskeleton is attached via a slack safety rope to



**Figure 5.** The Apptronik Sagittarius Exoskeleton used in this paper. The operator can climb stairs with the exoskeleton, even when it is not amplifying forces, due to the backdrivable torque-controlled actuators (gravity compensation and strength amplification are both active in the pictured movement). Coloring segregates rigid exoskeleton parts for the right leg (blue-through-purple), human interfaces (orange) and the safety features (red).

436 an overhead gantry system, and the rope’s height is operated by an assistant when the height is changing  
 437 rapidly (as in the stair-climbing activities pictured in Fig. 5. The operator wears a helmet, and there are  
 438 multiple easy ways to stop the exoskeleton in an emergency: 1) a software emergency stop button, 2)  
 439 a button on the top of the main backpack circuitry box, and 3) a button that the operator is required to hold at  
 440 all times.

## 441 6.2 Controller Implementation

442 While we have presented the controller design in a very general way, not all of its nuanced behavior is  
 443 relevant enough to demand implementation in the hardware system we used. In particular, the dynamic  
 444 terms in (34) were not large enough for the operator to notice their omission, and the dynamically consistent  
 445 pseudo-inversion of  $\mathbf{J}$  is unnecessary given that  $\mathbf{J}$  is invertible with the tasks we defined, thus

$$\mathbf{f} = \mathbf{J}^{-T}(\mathbf{g}_x - \mathbf{S}\boldsymbol{\tau}). \quad (40)$$

446 Note that when a component of the *amplification task* has  $K(s)$  set to zero, it will not amplify human  
 447 forces but will still compensate gravity.

448 To summarize the tasks of the controller, the six individual spatial force vector components of the  
 449 human-side force are fed into a diagonal matrix of amplification compensators as described in Sec. 3. And  
 450 this occurs in the frame of the *amplification task*—the hip frame. For the three sagittal plane forces and  
 451 torques ( $x$ -force,  $z$ -force, and  $y$ -torque) we may apply non-zero amplification, but the other three are left at  
 452 zero in this work. This is based on the physical intuition that the sagittal plane forces and torque represent  
 453 the larger interaction quantities during walking. This forms the 6-DOF *amplification task*. Based on a  
 454 bed of 12 insole-mounted pressure sensitive resistors, a rough estimate of the human center of pressure  
 455 is produced. This estimate is used to construct the elements of the *inter-foot force task*, which is also a  
 456 6-DOF task. With this hardware-specific preprocessing completed, the tasks are sent to a separate and more  
 457 generic module to perform the linear programming optimization work. The software implementation of  
 458 this optimization process is separate from the Apptronik control framework and is available as open source  
 459 software (Thomas, 2019). It primarily acts as a wrapper layer for the linear programming solver from the  
 460 COIN-OR (Lougee-Heimer, 2003) community.

### 461 6.3 Priorities

462 We avoided priority inversion events by iterative tuning of the priority weights (Tab. 5). This tuning  
 463 was done with squatting and stepping behaviors similar to the planned tests. High-priority tasks that were  
 464 never sacrificed held large weights. To save space in the limited numerical precision, these tasks were  
 465 ambiguously ranked relative to each other. The most important weights were quickly identified and set  
 466 to values that reliably avoided priority inversion in the tested behaviors. The more difficult question was  
 467 identifying the priorities preferred by the operator.

468 We iterated various priority rankings between the components of the *amplification task* until our operator  
 469 was satisfied with the behavior. First, we attempted to re-create linear inverted pendulum behavior by  
 470 prioritizing the moment components over the force components. This prioritization had been effective with  
 471 the Hume/Mercury biped robot (Kim et al., 2016, 2020). Unfortunately, this first approach frustrated the  
 472 operator, as the exoskeleton was naturally unstable. We eventually settled on the weightings in Tab. 5, which  
 473 sacrifice  $x$ -torque first and are more comfortable for the operator. This preference may be exoskeleton  
 474 or operator specific. The main drawback of the priorities from Tab. 5 is that at each stance transition  
 475 the hips of the device roll such that the stance hip is higher than the swing hip—likely due to the lower  
 476 penalty on hip amplification  $x$ -torque. However, we must sacrifice something, and this appeared to be the  
 477 least-uncomfortable choice. The large swing in the hip position is due to the rather loose coupling that the  
 478 backpack provides in this degree of freedom.

479 In testing, we began to suspect that operators may prefer a lower task penalty on the *inter-foot force task*  
 480 while in double support but react strongly negatively to *inter-foot force task* violation while in swing (since  
 481 this entails the exoskeleton loading their swing foot). We made a slight modification to the sum scalarized  
 482 cost for the *inter-foot force task* as described in (37a), (37d), (37e), and (38). A second copy of the task  
 483 penalty was added, with a dead zone. We made the *inter-foot force task* error appear *twice* in the task error  
 484 vector  $e(\tau)$  instead of only once as in (38). Thus, we had two separate components of the weight vector  $w$   
 485 from (37a) that penalized the same task. To introduce the dead zone for the second copy of the penalty,  
 486 we added a sparse bias vector to (37d) and (37e). We call this new penalty, with its dead zone and higher  
 487 penalty cost, the “Limit Penalty” (see Tab. 5) since it acts like a soft limit forcing the values to stay within  
 488 the dead zone. Within the dead zone, this new cost still behaves like the original weighted 1-norm cost  
 489 (plus a constant bias that does not influence the optimum), but at the boundary of the dead zone, the weight  
 490 suddenly becomes much higher.

Task	Weighting
Hip Amplification $x$ -Force	$1 \times 10^5$
Hip Amplification $y$ -Force	$1 \times 10^5$
Hip Amplification $z$ -Force	$1 \times 10^5$
Hip Amplification $x$ -Torque	$1 \times 10^0$
Hip Amplification $y$ -Torque	$1 \times 10^1$
Hip Amplification $z$ -Torque	$1 \times 10^5$
Inter-Foot $x$ -Force, Limit Penalty	$1 \times 10^{-1}, 1 \times 10^5$
Inter-Foot $y$ -Force, Limit Penalty	$1 \times 10^{-1}, 1 \times 10^5$
Inter-Foot $z$ -Force, Limit Penalty	$1 \times 10^{-6}, 1 \times 10^6$
Inter-Foot $x$ -Torque, Limit Penalty	$1 \times 10^{-6}, 1 \times 10^5$
Inter-Foot $y$ -Torque, Limit Penalty	$1 \times 10^{-6}, 1 \times 10^5$
Inter-Foot $z$ -Torque, Limit Penalty	$1 \times 10^0, 1 \times 10^5$

**Table 5.** Implemented Task Priorities

Test	SBC <sup>†</sup>	$\alpha_0$	Load
6.4.1	Off	0	0 N
6.4.2	On	0	0 N
6.4.3	On	0	110 N
6.4.4	On	3	110 N

†—Shared-Body Controller (SBC) enabled.

**Table 6.** Experimental Parameters

491 We scheduled the dead zone width based on the center of pressure location, such that in single support  
 492 this dead zone collapsed to zero and the *inter-foot force task* essentially took on the higher weighting of  
 493 the limit penalty. In dual support, the width of the dead zone reached its widest when the feet were evenly  
 494 balanced and reduced linearly in either direction away from that midpoint.

#### 495 6.4 Demonstrating the Amplification Task

496 We conducted a set of simple tests to demonstrate the difference between gravity compensation and  
 497 human strength amplification. These tests aimed to demonstrate an improvement in amplification stability  
 498 relative to previous controllers developed for the exoskeleton and its previous partial prototypes (the 1-DOF  
 499 testbed from (He et al., 2019; Thomas et al., 2019), a two degree of freedom leg, and a previous revision on  
 500 the same lower-body design) under the same project (Campbell, 2018), which was a condition of our using  
 501 the exoskeleton.<sup>9</sup>

502 Fig. 6 and Tab. 6 show the basic structure of our tests: the operator wears the exoskeleton in a roughly  
 503 standing position and various controller features are turned on and off. Extra weight is attached to the  
 504 backpack as an unknown load in tests 6.4.3-4, and the image shows where it hangs relative to the operator.  
 505 Fig. 7 shows the results of the three tests. This experimental condition and posture were chosen to avoid  
 506 singularity in the knees, prevent the actuators from overheating during the highest payload test, and  
 507 avoid reaching the friction limits of the foot contact, which could prevent complete satisfaction of the  
 508 amplification task.

<sup>9</sup> Which is to say, our testing time was limited, and the scope of our experiments was narrow.

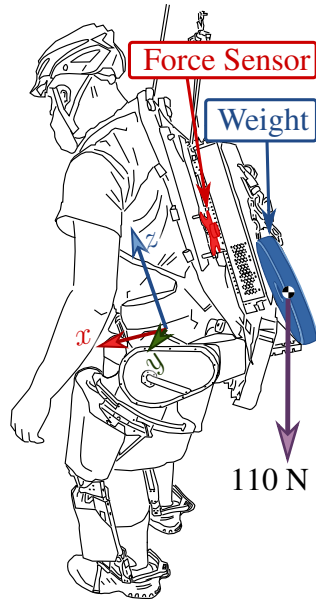


**Figure 6.** Load position in 6.4.3 and 6.4.4. Load hangs from a chain attached to the exoskeleton. Human effort measured with a six-axis force torque sensor, highlighted in red. Measurements are presented in the pictured “hip center” coordinate frame.

509 In the first test, 6.4.1 the exoskeleton joints are on, but the desired torque is zero. The first column of  
 510 plots in Fig. 7 show the large  $z$ -force on the backpack due to the gravitational load of the exoskeleton  
 511 acting on the operator. Variation in the angle shows that the operator was not perfectly holding still over  
 512 the duration of the test. This natural human movement, while it prevents us from easily comparing across  
 513 experiments (the operator does not even have the same resting posture between loading configurations), is  
 514 hard to compensate for or avoid.

515 The next test, 6.4.2 enables gravity compensation—which means the torques from the shared-body  
 516 controller are applied to the exoskeleton, but the amplification filters are all set to apply no strength  
 517 amplification feedback ( $\alpha_0 = 1$ , so  $\hat{f}_a = 0$ ). This drastically reduces, but does not entirely eliminate,  
 518 the interface forces and torques. Even if the exoskeleton’s mass parameters were perfectly modeled,  
 519 the operator would still need to apply forces through this interface to control the passive joints of the  
 520 exoskeleton. Compensating for the weight of the heavy exoskeleton is the most significant component of  
 521 the system’s behavior. We can see this from the enormous reduction in human interface forces and torques  
 522 in Fig. 7 between 6.4.1 and 6.4.2: the vertical force,  $F_z$ , drops roughly 300 Newtons, and the sagittal plane  
 523 torque,  $T_y$ , drops roughly 40 Newton meters.

524 In test 6.4.3, we added an 11 Kg (25 lb) mass to the backpack, without changing the control mode.  
 525 Based on our empirical determination, this represents the maximum load the exoskeleton could reliably  
 526 handle without overheating during dynamic motions like walking. The test does not focus on the transient  
 527 response but on the steady state behavior with the weight (mechanically, it would be hard to make the  
 528 weight addition appear sudden without dropping it).

529 We see some unexpected behavior in the vertical sensor force: the weight’s 110 N did not transfer to  
 530 the sensorized interface. The user confirmed that additional vertical force and sagittal torque were felt.  
 531 This suggests a “force leak” in the design of the backpack sensor, where the force of the added weight  
 532 is transferred to the operator without passing through the sensor. A likely culprit is the hip-pad of the  
 533 backpack (directly connected to the operator) and the hips of the exoskeleton—as this would be consistent

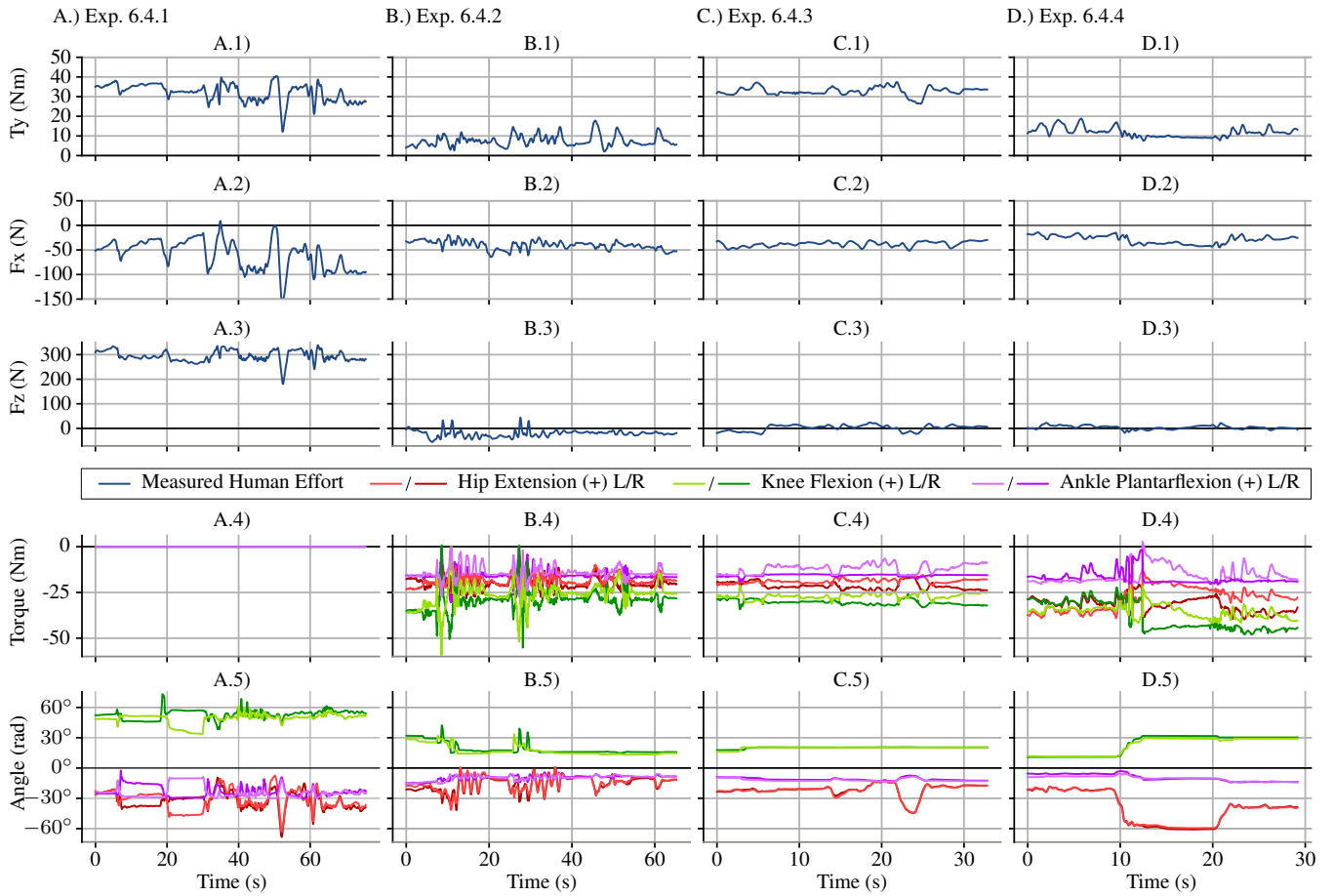


**Figure 7.** The four experiments from Tab. 6, shown as subfigure columns A–D, are compared in terms of the three sagittal plane components of the human–exoskeleton interaction force/torque, the sagittal joint torques, and the sagittal joint angles. In Exp. 6.4.1 (A), the exoskeleton joints apply no torque (as shown in A.4), and the human–exoskeleton interface supports  $\approx 300$  N (as shown in A.3) as well as a  $\approx 35$  Nm moment at the hip (as shown in A.1). In Exp. 6.4.2 (B), the controller is turned on with  $\alpha_0 = 1$  (no amplification), and human–exoskeleton vertical force (B.3) and sagittal torque (B.1) are vastly decreased due to gravity compensation. In Exp. 6.4.3 (C), a 11 kg mass is attached to the back of the exoskeleton (as shown in Fig. 6), and this produces an increase in the human–exoskeleton sagittal torque (C.1),  $\approx 30$  Nm. Finally, Exp. 6.4.4 (D) increases  $\alpha_0$  from 1 (no amplification) to 3 in the sagittal tasks, and the human–exoskeleton sagittal torque increase due to the added mass is reduced by roughly a third—considering B.1, C.1, and D.1 representing the average numerical value of the curves,  $D.1 - B.1 \approx 1/3(C.1 - B.1)$ —as expected. With the amplification engaged, the operator deepens the squat at 10 seconds (D.5) and then moves to a second, less extreme squat at 20 seconds (D.5), showing that the torque reduction continues to work. This squat is shown in the video attachment (Thomas, 2020). We would also expect that amplification would reduce the vertical force from the added mass; however, the vertical force remains roughly zero before adding the weight (B.3), after adding the weight (C.3), and with both the weight and amplification (D.3)—the expected 110 N force increase between (B.3) and (C.3) did not occur. Since the operator recalls feeling vertical forces from the addition of the mass, we suspect that there is a “force leak” where the vertical component transferred to the operator in a way the force sensor could not detect. Torque and angle measurements in the bottom two subfigure rows are measured using the exoskeleton’s spring deflection encoders and joint encoders, and therefore represent the exoskeleton’s—and not the operator’s—torque and position.

534 with the clear increase in the  $y$ -torque. The “force leak” does not appear to allow all vertical forces to  
 535 bypass the sensor. 6.4.1 clearly shows large forces.

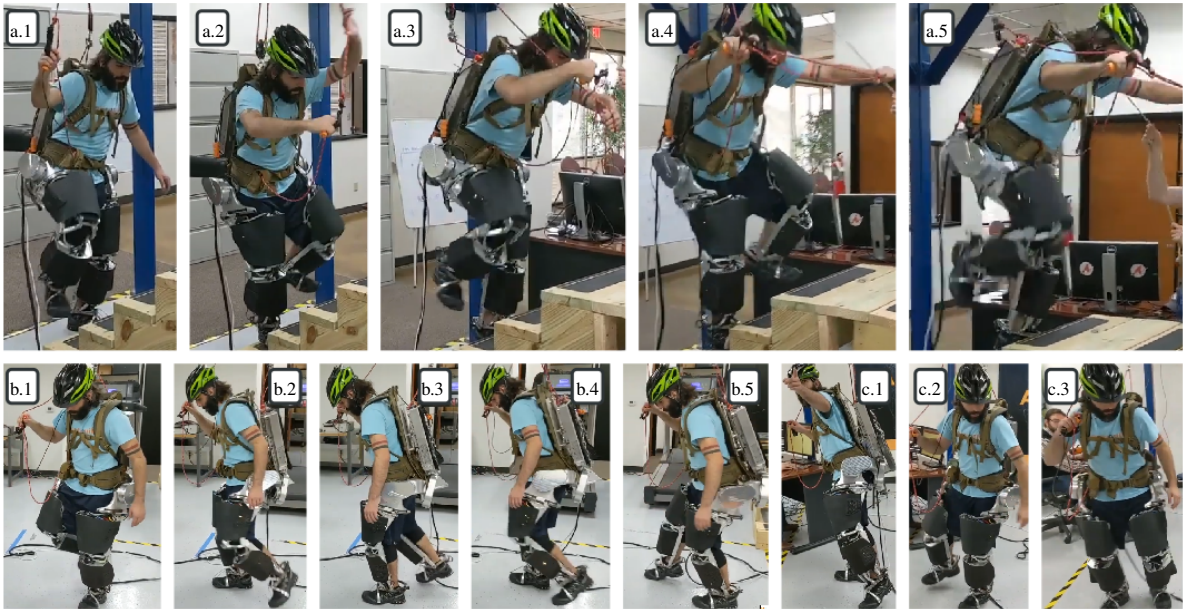


**Figure 8.** Frames from the demo. Frames a.1-5: climbing stairs with amplification but no added weight. Frames b.1-5: walking around. Frames c.1-3: walking around with amplification and extra weight.

536 In the final test, 6.4.4, we engaged the amplification filters—providing a steady state amplification factor  
 537 of 3, and a zero pair at 1 Hz for all three degrees of freedom in the sagittal plane. By choosing these  
 538 conservative settings, we were able to achieve stability on the first try.<sup>10</sup>

539 Our system is pioneering in that it amplifies human strength at the backpack/hip link of the exoskeleton;  
 540 there are no direct performance comparisons for this control feature. Our steady state amplification of human  
 541 forces by 300% exceeded the 208% amplification (52% mass reduction) of sagittal hip moment in (Zanotto  
 542 et al., 2015), which also used force feedback to amplify human lower-body strength. However, this is not an  
 543 exact comparison, as (Zanotto et al., 2015)'s system used a treadmill mounted exoskeleton, had a different  
 544 sensing configuration, and has only two degrees of freedom whereas our system has 12. The amplification's  
 545 pole frequency (.58 Hz) and amplification magnitude ( $\alpha_0 = 3$ ) at the hip/backpack human–exoskeleton  
 546 interface are comparable to our previous results on a 1-DOF human elbow exoskeleton; in the notation  
 547 of Appendix A, (He et al., 2019)'s robust controller used  $\alpha_0 = 10$ ,  $k_G = 0.1$ ,  $Z_g = 10$ , and  $P_g = 0.01$ ,  
 548 resulting in an amplification magnitude of 2.995 at 0.58 Hz. However, unlike our controller, (He et al.,  
 549 2019) had even greater amplification at lower frequencies: its lowest pole-pair was at 0.146 Hz, and its  
 550 steady state amplification rate was 9.91.

551 As shown in Fig. 7's fourth column, the human's effort was reduced to roughly a third of its value in  
 552 the third column in the  $y$ -torque component. More specifically, the disturbance due to the added weight,  
 553 which can be seen by comparing 6.4.3 (with weight) against 6.4.2 (no weight) in terms of  $y$ -axis torque, is  
 554 attenuated by the amplification factor, resulting in a much smaller disturbance effect when comparing 6.4.4  
 555 (attenuated weight) to 6.4.2 (no weight). We must make this comparison despite joint angle differences  
 556 on the order of 10 degrees between these tests—a limitation of our operator and operator–exoskeleton  
 557 coupling. In 6.4.4, the operator engages in two different squat positions (switching posture at roughly  
 558 10 and 20 seconds). The interface forces remain within 10-15 Nm despite these kinematic changes. This

<sup>10</sup> A later gain-tuning experiment revealed that the bandwidth limit is higher than this, but we ran out of time for exhaustive identification of this limit.

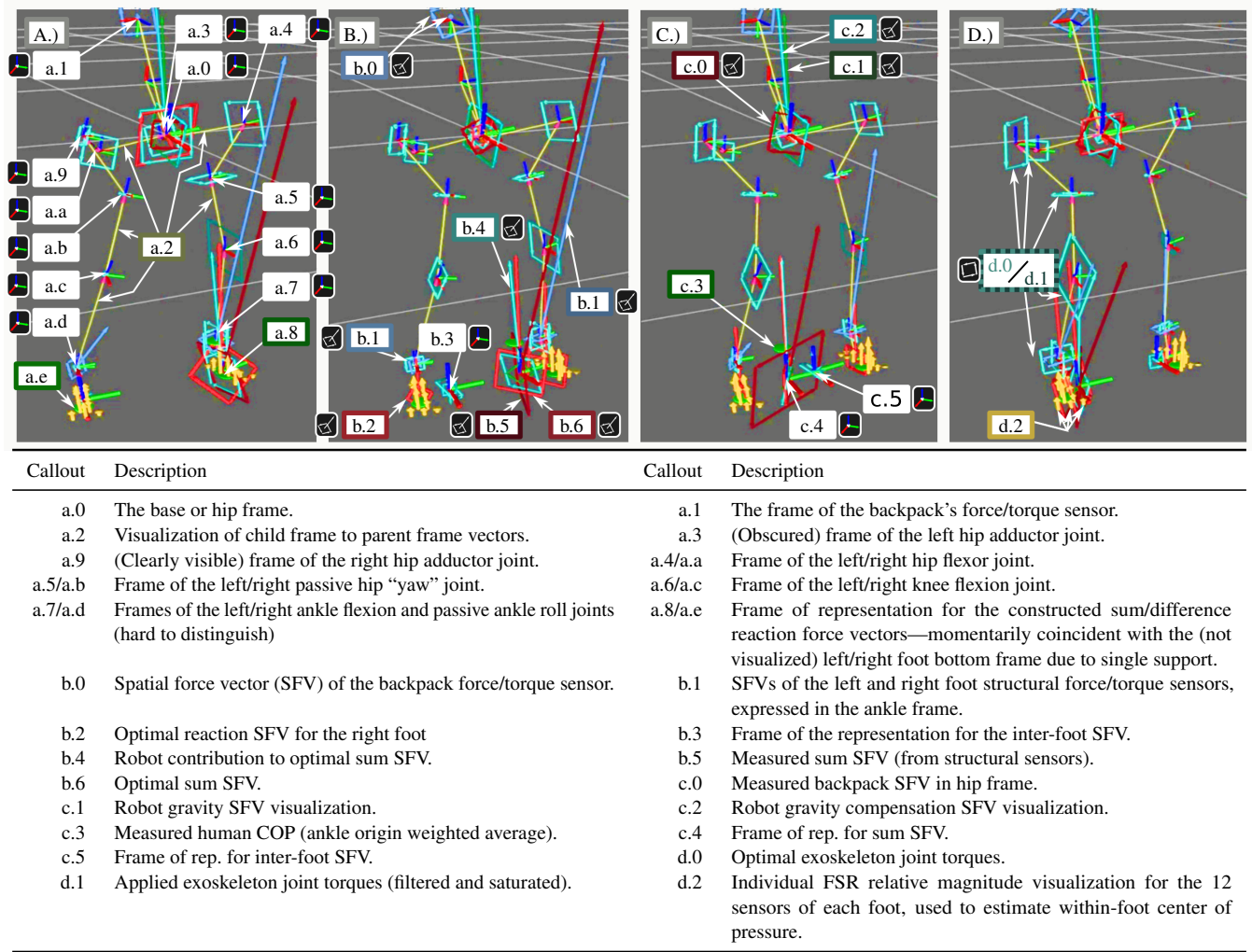


**Figure 9.** Human weight transfer in 0.2 seconds (subfigures evenly spaced in time) showing the exoskeleton visualization in the rviz program.

559 supports the notion that if the operator were able to perfectly reproduce the posture from Exp. 6.4.3 in  
 560 6.4.4, the y-axis torque would also be within this range.

## 561 6.5 Demonstrating Foot Transitions

562 Distributing weight between the two feet using the *inter-foot force task* is a key behavior of the system  
 563 and was tested when the operator walked on level ground and stairs. Since the exoskeleton itself was  
 564 based on high bandwidth torque-controlled actuation, the operator could easily backdrive it to climb up  
 565 stairs or to stand on one foot. While this happened, the exoskeleton continued to compensate for its own  
 566 gravitational weight and amplify strength at the hip/backpack sensor.

567 Fig. 8.b and Fig. 9 show the operator shifting weight from one foot to another and lifting up the legs one  
 568 at a time. Since the operator decreases the ground reaction force on a foot before lifting it, matching the  
 569 human ground reaction force distribution between the feet leads the exoskeleton to reduce its own ground  
 570 reaction force on that foot in anticipation of the loss of contact. As mentioned in Sec. 4, the weighting  
 571 matrices  $Q_1$  and  $Q_2$  in (15) are scheduled according to the exoskeleton's measurement of the human's  
 572 weight distribution. When the human shifts weight to one foot, the  $Q$  matrix penalty for reaction forces on

573 the other foot becomes much larger. And since this causes the COP of the exoskeleton to approximate the  
574 COP of the human, this prevents the human from needing to lift a load-bearing exoskeleton leg. In addition,  
575 the penalty limit method allowed the exoskeleton more freedom during dual support but smoothly reduced  
576 this freedom when approaching single support, so that by the time it was reached the *inter-foot force task*  
577 was essentially the highest priority.

578 This behavior is shown in more detail through the internal exoskeleton visualization of Fig. 9. This Rviz  
579 model visualizes many signals of interest, as described in the legend table. All frames are expressed as  
580 red ( $x$ ) green ( $y$ ) blue ( $z$ ) line segments meeting at the local origin. Spatial force vectors (comprising a  
581 force and a torque) are shown as a ray from the local origin (the force) and a bi-vector—a directed plane  
582 comprised of four vectors making a square—to represent the torque. Joint torques are represented as pure  
583 bi-vectors. Unlike vector descriptions of torque, the bi-vector visualization has an unambiguous scaling  
584 relative to the force visualizations and cannot be confused for them. The four instants pictured in Fig. 9  
585 of the contact transition show the apparent center of pressure moving from the left foot to the right foot,  
586 and the corresponding shift in all the joint torques and the predicted reaction forces from the shared-body  
587 controller. As this is shifting, the reference frame of expression for the sum of reaction forces and the  
588 *inter-foot force task*'s difference of reaction forces swap feet. At all times, the reaction force/torque b.6  
589 representing the sum is roughly equal to the sum ground reaction force calculated without using the passive  
590 joints b.4—which means that the exoskeleton is supporting the vast majority of its weight even during this  
591 transition. The backpack force/torque sensor b.0 confirms this, as it is small (and therefore hard to spot)  
592 throughout the transition.

## 7 DISCUSSION

593 Strength amplification control offers us the potential to feel stronger as we manipulate the load through  
594 our exoskeleton. This paper deploys a control that has put that vision into practice under laboratory  
595 circumstances.

### 596 7.1 Benefits and Drawbacks

597 This controller has several advantages relative to the state of the art. It respects contact limitations—  
598 guaranteeing that the exoskeleton will never force the person to roll their ankles, lift their toes, or slide their  
599 feet. It improves human-side admittance relative to the gravity compensation baseline without the anti-  
600 stable acceleration feedback of (Kazerooni et al., 2005). It keeps the human in control of the inter-foot force  
601 distribution using an elegant linear algebraic decomposition of the contact forces—a more general approach  
602 than Ref. (Jacobsen and Olivier, 2014). It allows the operator to move heavy objects without removing the  
603 force-feedback path that they would need in order to move the objects carefully—a force-feedback path  
604 that is removed by admittance control strategies (Fontana et al., 2014).

605 Of course, the controller has downsides as well. The strategy depends on centralizing the contact between  
606 the human and the exoskeleton into a small set of sensors.<sup>11</sup> This centralization places a significant burden  
607 on the mechanical design and introduces a new failure mode—the “force leak,” where interaction between  
608 the exoskeleton and the operator occurs outside the sensors. Additionally, all amplified interaction with  
609 the load must go through the exoskeleton structure—another mechanical design challenge. Due to the  
610 complexity of the mechanical design problem, the strategy makes it difficult to achieve the ultra-high  
611 energy density of successful locomotion augmentation exoskeletons (Kim et al., 2019; Mooney et al., 2014).

<sup>11</sup> With one foot on the ground, our exoskeleton measures the human at two places: the hip/backpack attachment and the swing foot attachment.

612 This is an open problem. Augmentation exoskeletons are already close to the energy-density boundary at  
613 which the energy they provide is equal to the energy they cost the user due to their mass. The extra design  
614 constraints make it harder for amplification exoskeletons to cross this boundary even at slow walking  
615 speeds.

## 616 7.2 Open Problems in the Control Framework

617 The control framework itself also has some open questions. First, we approximated the mechanical  
618 impedance of the human and the cuff as being component-wise decoupled between the six degrees of  
619 freedom in our *amplification task*. Since an extremely low amplification bandwidth is still stable, and  
620 since our tuning process increases bandwidth until instability is discovered, this approximation limits us  
621 by introducing conservatism in the final tuning. Because of inter-component human coupling behavior,  
622 the tuning process may result in a different answer depending on the order with which the individual task  
623 sub-component bandwidths are tuned.

624 Second, the framework was only tested with six *amplification task* sub-components. In theory, it supports  
625 arbitrarily many task sub-components. And it is also theoretically possible to join the *inter-foot force*  
626 *task* with the *amplification task*—to make the swing foot capable of acting like an amplified manipulator.  
627 Elimination of the inter-foot force  $f_d$  restricts the exoskeleton to applying a pair of ground reaction  
628 forces inside a six-dimensional space. The six-dimensional null space that is prohibited includes non-zero  
629 internal forces along the axis between the feet and canceling vertical torques perpendicular to the ground.  
630 Such internal forces and torques (Sentis et al., 2010) would be possible if the inter-foot force tasks were  
631 transformed into a second amplification task. And this would enable amplified kicking and manipulation  
632 of objects on the floor with the feet. We lacked the sensing configuration for such a test: it would require  
633 the full 6-DOF interaction force/torque between the human foot and the exoskeleton foot to be measured,  
634 rather than just the vertical pressure between them. Thus, to validate the scalability our theory predicts, we  
635 would need an exoskeleton with either A) more sensorized human contacts (arms, for example) or B) the  
636 elimination of all human–load contact that does not pass through the exoskeleton as an intermediary.

637 Third, the controller tuning process is intended to be robust to all activities the operator performs, but we  
638 cannot know all these activities beforehand. A practical extension to this work would be to introduce an  
639 always-online learning process to continually adapt the tuning and avoid instability. Previously we have  
640 looked at tuning automation using online stiffness estimation (Huang et al., 2020). However, this type of  
641 automation could potentially be simpler: if the system starts to vibrate, it could reduce the amplification  
642 bandwidth until the vibration subsides. Such a procedure would essentially automate our manual tuning  
643 approach.

644 On the other hand, higher performance might be obtained with a more complex strategy: modeling the  
645 human and redesigning the controller. Modeling the human online could exploit convex programs that  
646 automatically learn bounded-uncertainty models (Thomas and Sentis, 2019). With this more versatile  
647 system identification approach, even a human stiffness with ‘off-diagonal’ terms could be learned. With  
648 every change to the model of the human stiffness bounds, robust control theory could synthesize a transfer  
649 matrix  $\mathbf{K}(s)$  that guarantees stability.

650 Relating to the approximate lexicographic optimization using the 1-norm cost, other cost functions  
651 could also be considered. In particular, a 2-norm cost approach could smoothly transition through priority  
652 inversion events—improving over the hard-switching behavior of the 1-norm cost. Such a cost has been  
653 explored in (Campbell, 2018) for this exoskeleton and in (Kim et al., 2020) for biped robots. However this  
654 cost obfuscates the realized task priorities, which hindered efforts to understand the required sacrifices

655 when designing the cost. Perhaps a generalizing compromise exists in costs that are locally quadratic, but  
656 asymptotically linear.

657 Finally, the approach makes an assumption that a foot is always on the ground—and this precludes  
658 interesting applications in free-fall, underwater (with neutral buoyancy), or micro-gravity. In such  
659 circumstances, the *amplification task* and *inter-foot force task* structures would need to be combined  
660 together and significantly altered. A “virtual single foot contact” would not exist. In its place, the *change*  
661 *in centroidal momentum* (Koolen et al., 2016) would need to become the component of torque-space left  
662 intentionally unconstrained by the tasks. The remaining DOFs in torque-space would then be the subject of  
663 the new combined amplification task. The assignment of intuitive and easy-to-tune amplification controllers  
664 to such a task—which would concern an ever-changing subspace of the end effector contact force space—is  
665 an open problem. However, the approach to parameterizing the *internal forces of multi-contact* from (Sentis  
666 et al., 2010) would be a reasonable starting point.

### 667 7.3 Series Elastic Actuators

668 Our exoskeleton hardware features series elastic actuators that are force/torque-controlled, and this  
669 decision also comes with benefits and drawbacks. To our knowledge, this paper is the first demonstration  
670 of Multi-DOF amplification control based on human interface force sensors and actuator force sensors (i.e.  
671 the series elastic elements). While such actuators are commonly used in wearable robots, they are a key  
672 part of our strategy, because with them we can avoid sensorizing the external force interface. This is a  
673 major advantage compared to systems designed to follow the extender concept (Kazerooni and Guo, 1993).  
674 The lack of load sensors gives us the freedom to properly handle amplification for load contract forces at  
675 any contact point along the structure of the exoskeleton.

676 As for series compliance itself, however, control performance would be *better* with nearly-rigid springs.  
677 In our experiment, the primary bandwidth-limiting factor that  $\eta(s)$  must describe is the 10 Hz bandwidth of  
678 the exoskeleton’s actuators. And this bandwidth is limited by the mechanical stiffness of the series spring,  
679 the noise level in the motor position and spring deflection sensors, and the bandwidth of the electrical  
680 current controller. The time-delay of approximately 1 ms was non-limiting, so to improve the overall  
681 performance of the exoskeleton, the most efficient strategy would be to increase the spring stiffness and  
682 spring deflection sensor resolution. The series elastic actuators are simply torque sources to us, and direct  
683 drive motors offer higher bandwidth as torque sources. Removing the springs could also save weight. But  
684 series elasticity has some practical advantages: the force sensing is cheap and high quality, the exoskeleton’s  
685 motors are protected from impacts, and both the transmission’s friction and the rotor’s reflected inertia are  
686 well hidden from the user.

### 687 7.4 Potential Applications

688 We have demonstrated the control framework on the Apptronik Sagittarius exoskeleton, which is designed  
689 to lift heavy payloads as the user moves quickly. In this use case, the benefit of amplification control—  
690 relative to gravity compensation of the payload—is the potential reduction of inertial forces the user  
691 needs to compensate (without resorting to acceleration feedback) and the forces due to modeling error in  
692 the compensation. Future controllers for this application might investigate further enhancements to the  
693 operator’s quality of life, such as posture or safety support that guides the user.

694 However, amplification is also of great interest in load manipulation and heavy-duty tool use. We imagine  
695 some industrial amplification exoskeletons might be for slowly manipulating very large loads under direct  
696 human control. If they were to move fast, they would require significantly more impressive power density

than we typically see today. Such an exoskeleton, worn by a skilled operator, might be fielded in difficult terrain as an alternative to tracked construction vehicles, perhaps with specialized tools for manipulating the environment. Given the strength of the system, these tools might not be constrained by weight relative to other tools for such difficult environments. The exoskeleton could act as an adjustable bracing system that allows the operator to maneuver them into position in a controlled way. For example, a construction worker could use an exoskeleton to maneuver an oversize pneumatic drill to carve a staircase on un-finished mountain terrain. Exoskeletons as platforms offer new possibilities for industrial tools and potential job sites by combining the flexibility of people with the strength of machines.

While our exoskeleton is designed to mimic the kinematics of the person wearing it, this is not the only way to approach the design. The control framework also has the potential to allow non-anthropomorphic exoskeletons to amplify human interaction. For example, consider a robot connected to an operator's feet with long spindly legs that join together at a robot 'hip'. Where this hip also features an enormous power tool that requires the user to manipulate it with both hands. Such an architecture would require the same control system features as our anthropomorphic exoskeleton structure: strength amplification in the frame of the robot's hip, awareness of contact inequalities, and human-led footstep transitions.

## ACKNOWLEDGMENT

For this research in human strength amplification, Apptronik Systems Inc. provided, at no cost, access to their exoskeleton hardware called Sagit-P5. They also provided mechanical maintenance and improvements to the low level interfaces to facilitate the testing. The authors would like to thank Donghyun Kim for providing insights on contact transitions. This system was designed and built by a team including Jonas Fox, Brad Resh, Uday Savaria, Ryan Harkins, Ryan MacWilliams, Joel Cox, and Paul Fleury. The authors would also like to acknowledge Bill Helmsing and Jeff Cardenas for allocating time for our research on the Sagit-P5 exoskeleton.

This work was supported in part by NASA grant NNX15AQ33H "Controlling Robots with a Spring in Their Step," for which Gray Thomas is the fellow and Luis Sentis is the advisor and by two STTR grants from the US Department of Defense.

## REFERENCES

- Adams, R. J. and Hannaford, B. (1999). Stable haptic interaction with virtual environments. *IEEE Transactions on Robotics and Automation* 15, 465–474
- Agrawal, A., Harib, O., Hereid, A., Finet, S., Masselin, M., Praly, L., et al. (2017). First steps towards translating hzd control of bipedal robots to decentralized control of exoskeletons. *IEEE Access* 5, 9919–9934
- Bouyarmane, K. and Kheddar, A. (2017). On weight-prioritized multitask control of humanoid robots. *IEEE Transactions on Automatic Control* 63, 1632–1647
- Bretl, T. and Lall, S. (2008). Testing static equilibrium for legged robots. *IEEE Transactions on Robotics* 24, 794–807
- Brissonneau, N., He, B., Thomas, G. C., and Sentis, L. (2021). Biologically-inspired impedance control with hysteretic damping. *IEEE Control Systems Letters* 5, 1717–1722. doi:10.1109/LCSYS.2020.3044101
- Buerger, S. P. and Hogan, N. (2006). Relaxing passivity for human-robot interaction. In *Intelligent Robots and Systems (IROS), 2006 IEEE/RSJ International Conference on* (IEEE), 4570–4575

- 736 Buerger, S. P. and Hogan, N. (2007). Complementary stability and loop shaping for improved human–robot  
737 interaction. *IEEE Transactions on Robotics* 23, 232–244. doi:10.1109/TRO.2007.892229
- 738 Campbell, O. H., IV (2018). *Framework for Full Body Augmentative Exoskeleton Control*. Master's thesis,  
739 The University of Texas at Austin
- 740 Candes, E. J., Wakin, M. B., and Boyd, S. P. (2008). Enhancing sparsity by reweighted  $\ell_1$  minimization.  
741 *Journal of Fourier analysis and applications* 14, 877–905
- 742 Colgate, J. E. and Brown, J. M. (1994). Factors affecting the z-width of a haptic display. In *Robotics and  
743 Automation, 1994. Proceedings., 1994 IEEE International Conference on* (IEEE), 3205–3210
- 744 Colgate, J. E. and Hogan, N. (1988). Robust control of dynamically interacting systems. *International  
745 Journal of Control* 48, 65–88
- 746 Featherstone, R. (2014). *Rigid body dynamics algorithms* (Springer)
- 747 Fontana, M., Vertechy, R., Marcheschi, S., Salsedo, F., and Bergamasco, M. (2014). The body extender:  
748 A full-body exoskeleton for the transport and handling of heavy loads. *IEEE Robotics & Automation  
749 Magazine* 21, 34–44
- 750 Gonzalez, D. J. and Asada, H. H. (2019). Hybrid open-loop closed-loop control of coupled human–robot  
751 balance during assisted stance transition with extra robotic legs. *IEEE Robotics and Automation Letters*  
752 4, 1676–1683
- 753 He, B., Huang, H., Thomas, G. C., and Sentis, L. (2019). Complex stiffness model of physical human–robot  
754 interaction: Implications for control of performance augmentation exoskeletons. In *2019 IEEE/RSJ  
755 International Conference on Intelligent Robots and Systems (IROS)* (IEEE), 6748–6755
- 756 He, B., Huang, H., Thomas, G. C., and Sentis, L. (2020). A complex stiffness human impedance model with  
757 customizable exoskeleton control. *IEEE Transactions on Neural Systems and Rehabilitation Engineering*  
758 28, 2468–2477
- 759 He, B., Thomas, G. C., Paine, N., and Sentis, L. (2019). Modeling and loop shaping of single-joint  
760 amplification exoskeleton with contact sensing and series elastic actuation. In *2019 Annual American  
761 Control Conference (ACC)*. AACC (IEEE), 4580–4587
- 762 Hogan, N. (1984). Adaptive control of mechanical impedance by coactivation of antagonist muscles. *IEEE  
763 Transactions on Automatic Control* 29, 681–690
- 764 Hogan, N. (1989). Controlling impedance at the man/machine interface. In *Robotics and Automation  
765 (ICRA), 1989 IEEE International Conference on* (IEEE), 1626–1631
- 766 Huang, H., Cappel, H., Thomas, G. C., He, B., and Sentis, L. (2020). In *2020 Annual American Control  
767 Conference (ACC)*. AACC (IEEE), 5131–5138
- 768 Jacobsen, S. C. and Olivier, M. X. (2014). *Contact displacement actuator system*. US Patent 8,849,457
- 769 Kawamoto, H. and Sankai, Y. (2005). Power assist method based on phase sequence and muscle force  
770 condition for hal. *Advanced Robotics* 19, 717–734
- 771 Kazerooni, H. (1990). Human–robot interaction via the transfer of power and information signals. *IEEE  
772 Transactions on Systems, Man, and Cybernetics* 20, 450–463
- 773 Kazerooni, H. (2005). Exoskeletons for human power augmentation. In *Intelligent Robots and Systems  
774 (IROS), 2005 IEEE/RSJ International Conference on* (IEEE), 3459–3464
- 775 Kazerooni, H. and Guo, J. (1993). Human extenders. *Journal of Dynamic Systems, Measurement, and  
776 Control* 115, 281–290
- 777 Kazerooni, H. and Mahoney, S. (1991a). Dynamics and control of robotic systems worn by humans. In  
778 *Proceedings. 1991 IEEE International Conference on Robotics and Automation* (IEEE), 2399–2405
- 779 Kazerooni, H. and Mahoney, S. L. (1991b). Dynamics and control of robotic systems worn by humans.  
780 *Journal of Dynamic Systems, Measurement, and Control* 113, 379–387. doi:10.1115/1.2896421

- 781 Kazerooni, H., Racine, J.-L., Huang, L., and Steger, R. (2005). On the control of the berkeley lower  
782 extremity exoskeleton (BLEEX). In *Robotics and Automation (ICRA), 2005 IEEE International  
783 Conference on* (IEEE), 4353–4360
- 784 Kim, B. and Deshpande, A. D. (2017). An upper-body rehabilitation exoskeleton harmony with  
785 an anatomical shoulder mechanism: Design, modeling, control, and performance evaluation. *The  
786 International Journal of Robotics Research* 36, 414–435
- 787 Kim, D., Jorgensen, S. J., Hwang, H., and Sentis, L. (2018). Control scheme and uncertainty considerations  
788 for dynamic balancing of passive-ankled bipeds and full humanoids. In *2018 IEEE-RAS 18th  
789 International Conference on Humanoid Robots (Humanoids)* (IEEE), 1–9
- 790 Kim, D., Jorgensen, S. J., Lee, J., Ahn, J., Luo, J., and Sentis, L. (2020). Dynamic locomotion for  
791 passive-ankle biped robots and humanoids using whole-body locomotion control. *The International  
792 Journal of Robotics Research* 39, 936–956
- 793 Kim, D., Zhao, Y., Thomas, G. C., Fernandez, B. R., and Sentis, L. (2016). Stabilizing series-elastic  
794 point-foot bipeds using whole-body operational space control. *IEEE Transactions on Robotics* 32,  
795 1362–1379
- 796 Kim, J., Lee, G., Heimgartner, R., Arumukhom Revi, D., Karavas, N., Nathanson, D., et al. (2019).  
797 Reducing the metabolic rate of walking and running with a versatile, portable exosuit. *Science* 365,  
798 668–672. doi:10.1126/science.aav7536
- 799 Kong, K., Moon, H., Jeon, D., and Tomizuka, M. (2010). Control of an exoskeleton for realization of  
800 aquatic therapy effects. *IEEE/ASME Transactions on Mechatronics* 15, 191–200
- 801 Kong, K. and Tomizuka, M. (2009). Control of exoskeletons inspired by fictitious gain in human model.  
802 *IEEE/ASME Transactions on Mechatronics* 14, 689–698
- 803 Koolen, T., Bertrand, S., Thomas, G. C., De Boer, T., Wu, T., Smith, J., et al. (2016). Design of a  
804 momentum-based control framework and application to the humanoid robot Atlas. *International Journal  
805 of Humanoid Robotics* 13, 1650007
- 806 Kwa, H. K., Noorden, J. H., Missel, M., Craig, T., Pratt, J. E., and Neuhaus, P. D. (2009). Development of  
807 the IHMC mobility assist exoskeleton. In *Robotics and Automation (ICRA), 2009 IEEE International  
808 Conference on* (IEEE), 2556–2562
- 809 Lecours, A., St-Onge, B. M., and Gosselin, C. (2012). Variable admittance control of a four-degree-  
810 of-freedom intelligent assist device. In *Robotics and Automation (ICRA), 2012 IEEE International  
811 Conference on* (IEEE), 3903–3908
- 812 Lin, J., Lv, G., and Gregg, R. D. (2019). Contact-invariant total energy shaping control for powered  
813 exoskeletons. In *2019 American Control Conference (ACC)* (AACC), 664–670
- 814 Lougee-Heimer, R. (2003). The common optimization interface for operations research: Promoting  
815 open-source software in the operations research community. *IBM Journal of Research and Development*  
816 47, 57–66
- 817 Lv, G., Zhu, H., and Gregg, R. D. (2018). On the design and control of highly backdrivable lower-limb  
818 exoskeletons: A discussion of past and ongoing work. *IEEE Control Systems Magazine* 38, 88–113
- 819 Makinson, J. B., Bodine, D. P., and Fick, B. R. (1969). *Machine augmentation of human strength and  
820 endurance Hardiman I prototype project*. Tech. rep., Specialty Materials Handling Products Operation,  
821 General Electric Company
- 822 Mooney, L. M., Rouse, E. J., and Herr, H. M. (2014). Autonomous exoskeleton reduces metabolic cost of  
823 human walking during load carriage. *Journal of neuroengineering and rehabilitation* 11, 80
- 824 Mungai, M. E. and Grizzle, J. (2020). Feedback control design for robust comfortable sit-to-stand motions  
825 of 3d lower-limb exoskeletons. *IEEE Access*

- 826 Paine, N., Mehling, J. S., Holley, J., Radford, N. A., Johnson, G., Fok, C.-L., et al. (2015). Actuator control  
827 for the NASA-JSC Valkyrie humanoid robot: A decoupled dynamics approach for torque control of  
828 series elastic robots. *Journal of Field Robotics* 32, 378–396
- 829 Paine, N., Oh, S., and Sentis, L. (2014). Design and control considerations for high-performance series  
830 elastic actuators. *IEEE/ASME Transactions on Mechatronics* 19, 1080–1091
- 831 Paine, N. A. (2014). *High-performance series elastic actuation*. Ph.D. thesis, The University of Texas at  
832 Austin
- 833 Radford, N. A., Strawser, P., Hambuchen, K., Mehling, J. S., Verdeyen, W. K., Donnan, A. S., et al. (2015).  
834 Valkyrie: NASA's first bipedal humanoid robot. *Journal of Field Robotics* 32, 397–419
- 835 Sawicki, G. S., Beck, O. N., Kang, I., and Young, A. J. (2020). The exoskeleton expansion: improving  
836 walking and running economy. *Journal of neuroengineering and rehabilitation* 17, 1–9
- 837 Sentis, L., Park, J., and Khatib, O. (2010). Compliant control of multicontact and center-of-mass behaviors  
838 in humanoid robots. *Robotics, IEEE Transactions on* 26, 483–501
- 839 Stephens, B. J. and Atkeson, C. G. (2010). Dynamic balance force control for compliant humanoid  
840 robots. In *2010 IEEE/RSJ International Conference on Intelligent Robots and Systems*. 1248–1255.  
841 doi:10.1109/IROS.2010.5648837
- 842 Sugar, T. G., He, J., Koeneman, E. J., Koeneman, J. B., Herman, R., Huang, H., et al. (2007). Design  
843 and control of RUPERT: a device for robotic upper extremity repetitive therapy. *IEEE transactions on*  
844 *neural systems and rehabilitation engineering* 15, 336–346
- 845 Thomas, G. C. (2019). *LP Exo: A free implementation of a 1-Norm Prioritized Whole Body Controller*.  
846 GitHub, [https://bitbucket.org/gray\\_thomas/exo\\_lp.git](https://bitbucket.org/gray_thomas/exo_lp.git)
- 847 Thomas, G. C. (2020). *Implementation of "An Amplification Shaping Framework for Exoskeletal Human*  
848 *Strength Augmentation"*. Youtube. [https://youtu.be/rcDMHYgGV\\_4](https://youtu.be/rcDMHYgGV_4)
- 849 Thomas, G. C., Coholich, J. M., and Sentis, L. (2019). Compliance shaping for control of strength  
850 amplification exoskeletons with elastic cuffs. In *Proceedings of the 2019 IEEE/ASME International*  
851 *Conference on Advanced Intelligent Mechatronics* (IEEE and ASME), 1199–1206
- 852 Thomas, G. C. and Sentis, L. (2019). Quadric inclusion programs: an lmi approach to  $\mathcal{H}_\infty$ -model  
853 identification. *IEEE Transactions on Automatic Control* 64, 4229–4236. doi:10.1109/TAC.2019.2897886
- 854 Young, A. J. and Ferris, D. P. (2016). State of the art and future directions for lower limb robotic  
855 exoskeletons. *IEEE Transactions on Neural Systems and Rehabilitation Engineering* 25, 171–182
- 856 Yu, W. and Rosen, J. (2013). Neural PID control of robot manipulators with application to an upper limb  
857 exoskeleton. *IEEE Transactions on Cybernetics* 43, 673–684
- 858 Zanotto, D., Akiyama, Y., Stegall, P., and Agrawal, S. K. (2015). Knee joint misalignment in exoskeletons  
859 for the lower extremities: Effects on user's gait. *IEEE Transactions on Robotics* 31, 978–987
- 860 Zhang, J., Fiers, P., Witte, K. A., Jackson, R. W., Poggensee, K. L., Atkeson, C. G., et al. (2017).  
861 Human-in-the-loop optimization of exoskeleton assistance during walking. *Science* 356, 1280–1284